

INFORMATION TO USERS

This manuscript has been reproduced from the microfilm master. UMI films the text directly from the original or copy submitted. Thus, some thesis and dissertation copies are in typewriter face, while others may be from any type of computer printer.

The quality of this reproduction is dependent upon the quality of the copy submitted. Broken or indistinct print, colored or poor quality illustrations and photographs, print bleedthrough, substandard margins, and improper alignment can adversely affect reproduction.

In the unlikely event that the author did not send UMI a complete manuscript and there are missing pages, these will be noted. Also, if unauthorized copyright material had to be removed, a note will indicate the deletion.

Oversize materials (e.g., maps, drawings, charts) are reproduced by sectioning the original, beginning at the upper left-hand corner and continuing from left to right in equal sections with small overlaps. Each original is also photographed in one exposure and is included in reduced form at the back of the book.

Photographs included in the original manuscript have been reproduced xerographically in this copy. Higher quality 6" x 9" black and white photographic prints are available for any photographs or illustrations appearing in this copy for an additional charge. Contact UMI directly to order.

U·M·I

University Microfilms International
A Bell & Howell Information Company
300 North Zeeb Road, Ann Arbor, MI 48106-1346 USA
313/761-4700 800/521-0600

Order Number 9408510

Physics of semiconductor microcavity lasers

Boggavarapu, Deepak, Ph.D.

The University of Arizona, 1993

U·M·I
300 N. Zeeb Rd.
Ann Arbor, MI 48106

PHYSICS OF SEMICONDUCTOR MICROCAVITY LASERS

by

Deepak Boggavarapu

A Dissertation Submitted to the Faculty of the
COMMITTEE ON OPTICAL SCIENCES (GRADUATE)

In Partial Fulfillment of the Requirements

For the Degree of

DOCTOR OF PHILOSOPHY

In the Graduate College

THE UNIVERSITY OF ARIZONA

1993

THE UNIVERSITY OF ARIZONA
GRADUATE COLLEGE

As members of the Final Examination Committee, we certify that we have read the dissertation prepared by Deepak Boggavarapu entitled Physics of Semiconductor microcavity lasers

and recommend that it be accepted as fulfilling the dissertation requirement for the Degree of Doctor of Philosophy

Hyatt Gibbs Hyatt M. Gibbs 8/17/93

Date

Nasser Peyghambarian Nasser Peyghambarian 8/17/93

Date

Richard C. Powell Richard C. Powell 8/17/93

Date

Date

Date

Final approval and acceptance of this dissertation is contingent upon the candidate's submission of the final copy of the dissertation to the Graduate College.

I hereby certify that I have read this dissertation prepared under my direction and recommend that it be accepted as fulfilling the dissertation requirement.

Hyatt Gibbs Hyatt M. Gibbs 8/17/93
Dissertation Director Date

STATEMENT BY AUTHOR

This dissertation has been submitted in partial fulfillment of requirements for an advanced degree at The University of Arizona and is deposited in the University Library to be made available to borrowers under rules of the Library.

Brief quotations from this dissertation are allowable without special permission, provided that accurate acknowledgement of source is made. Requests for permission for extended quotation from or reproduction of this manuscript in whole or in part may be granted by the head of the major department or the Dean of the Graduate College when in his or her judgement the proposed use of the material is in the interests of scholarship. In all other instances, however, permission must be obtained from the author.

SIGNED: 

ACKNOWLEDGEMENTS

The technical portion of this journey is documented in the pages that follow; however, it is the people encountered along the way that have made it memorable. Only this short space is allowed to thank them. The evolution from my first meeting with Professor H. M. Gibbs, the noted optical physicist, to eventually getting to know The Flying Count Gibbsupov has been a unique experience. Watching him delve to the heart of a problem and look for a simple physical explanation has taught me something of the way physics should be done. I have benefitted greatly from many discussions with Professor Pierre Meystre, whose openness and insight have helped to clarify concepts and broaden my view of physics. Professor Galina Khitrova's gallium arsenide recipes and her many hours spent tending the pot (MBE machine) resulted in the VCSEL samples used in this work.

From my colleagues in the lab I have learned the most about experimental work. Three comrades in particular stand out: Chih-li Chuang, whose advice and friendship during my first year was invaluable; Jeff Grantham, from whom I learned a great deal about actual lab techniques and a little about discipline; Ruxiang Jin, who is always seeking new experiments to try and with whom most of this work was carried out. The international character of the group has allowed me to gain some insights into different cultures. Those that have passed through during this time have come from Korea, Taiwan, China, Japan, Russia, France, and Norway. Even the blandness of America has been spiced by influences from the Deep South and more recently by transplanted Minnesotans. Ron Roncone, Brian McGinnis, and Ken Meissner have introduced me to new diversions of mountain biking, skiing, and Mexico beach camping trips.

Throughout everything, most important has been my family. My older brother Jagadish has kept me up to date with the latest sports news throughout the last four years. My younger brother Sajiv has always been willing to listen, while patiently putting up with living with me for the last four years. The love and support of my mother and father have helped me overcome many obstacles along the way. Without them, this work would never have been completed.

To my parents

TABLE OF CONTENTS

LIST OF ILLUSTRATIONS.....	8
ABSTRACT	10
INTRODUCTION.....	11
1. MICROCAVITY LASER WITH INJECTED SIGNAL	14
Instabilities with Weak Injected Signal	14
Introduction.....	14
Experimental Method.....	15
Results.....	18
Theoretical Model.....	23
Summary	27
Asymmetric Local Gain Modification	27
Introduction.....	27
Experimental Method.....	28
Experimental Evidence	30
Discussion.....	38
Summary	45
2. CHARACTERISTICS OF MICROCAVITY LASERS	47
Linewidth Enhancement Factor	47
Introduction.....	47
Experimental Method.....	49
Analysis	50
Summary	54
Below Threshold Behavior	55
Introduction.....	55
Experimental Method and Analysis	56
Results and Discussion.....	58
Summary	67

TABLE OF CONTENTS - *Continued*

3. PHOTON NUMBER CORRELATIONS NEAR THRESHOLD.....	68
Introduction	68
Theoretical Background	73
Experimental Method.....	79
Results and Discussion.....	84
Summary	90
CONCLUSION	91
REFERENCES.....	94

LIST OF ILLUSTRATIONS

Figure	Page
I.1 Schematic of VCSEL structure and typical reflectivity curve	12
1.1 Experimental setup to investigate injection behavior.....	19
1.2 Sequence of frequency spectra for positive detuning.....	20
1.3 Sequence of frequency spectra for negative detuning.....	22
1.4 Injection locking range versus reciprocal injection power.....	24
1.5 Theoretically computed frequency spectra and phase portraits.....	26
1.6 High injection power modified VCSEL frequency spectra	31
1.7 Pushing and quenching of VCSEL lasing with increasing injection	33
1.8 Experimentally determined shape for asymmetric gain modification ...	34
1.9 High injection sequence of frequency spectra	37
1.10 Shift of new frequency as a function of injection power	39
1.11 Relaxation oscillations around the newly generated frequency.....	40
1.12 Theoretical curve of asymmetric local gain modification	44
2.1 VCSEL laser linewidth versus reciprocal pump power	51
2.2 Theoretical calculation of linewidth enhancement factor	53
2.3 Measured λ_0 and $\Delta\lambda$ of Fabry-Perot resonance below threshold.....	59
2.4 Refractive index change deduced from Fabry-Perot shift.....	61
2.5 Absorption as a function of carrier density	63

LIST OF ILLUSTRATIONS - *Continued*

Figure	Page
2.6 Carrier lifetime as a function of density	66
3.1 Output power versus pump power for various β	72
3.2 Experimental setup used to measure photon number correlations.....	80
3.3 Experimental and theoretical comparison of correlation function.....	85
3.4 Theoretical plots of correlation function for large β	87
3.5 Second order coherence function for various values of β	89

ABSTRACT

The development of the microcavity laser has opened new vistas for exploration in regard to light-matter interaction. Here, we consider several experimental investigations with these smallest of lasers. Injection of an external optical signal into a vertical cavity surface emitting laser (VCSEL) reveals the weak injection regime of frequency locking and the strong injection regime of asymmetric local modification to the semiconductor gain curve. Above laser threshold linewidth measurements allow us to determine the linewidth enhancement factor, in agreement with theory. Below threshold measurements allow us to deduce carrier density and carrier lifetime. The definition of laser threshold in a microcavity laser has recently come under question. Intensity correlation measurements of the light emitted by a VCSEL exhibit a peak at laser threshold. Theoretical calculations confirm the experimental data and further show that this threshold peak remains even as the spontaneous emission rate into nonlasing modes approaches zero.

INTRODUCTION

Light. Matter. Cavity. The essence of our investigations is embodied in these three words. The (optical) cavity we consider is one of the smallest ever made. The matter of our interest is the semiconductor gallium arsenide. The process of light emission is our central focus. The physics of the interplay between light and matter (gallium arsenide gain medium) immersed in a high finesse optical cavity (microcavity) is the problem we study.

Before continuing, we must explain - *What is a microcavity laser?* The microcavity laser is the latest evolutionary step in progress since the birth of the laser [Maiman (1960)]. Specifically, we consider an active gain region length on the order of the light emission wavelength. Typical cavity lengths we have worked with include 1λ , 3λ , and 9λ (where $\lambda \sim 880$ nm). Cavity mirrors consist of distributed Bragg reflectors (i.e. quarterwave stacks) of alternating high (GaAs) and low (AlAs) refractive index material. The fact that the gain medium and mirrors can be grown as an integrated structure by molecular beam epitaxy (MBE) has led to an explosion of work in this field (for a recent review see Jewell et al. (1991)). The particular type of semiconductor microcavity laser we have just described is known as the vertical cavity surface emitting laser (VCSEL), with a typical structure shown in Fig. I.1a (for a more detailed discussion of design issues, see Chuang (1991) and references therein). The large number of mirror layers ensures a band of very high reflectivity and the short active region length ensures that only a single longitudinal mode exists within the mirror stop band and the semiconductor gain region. A typical calculated linear reflectivity curve for a VCSEL is shown in Fig. I.1b, with a single Fabry-Perot resonance dip

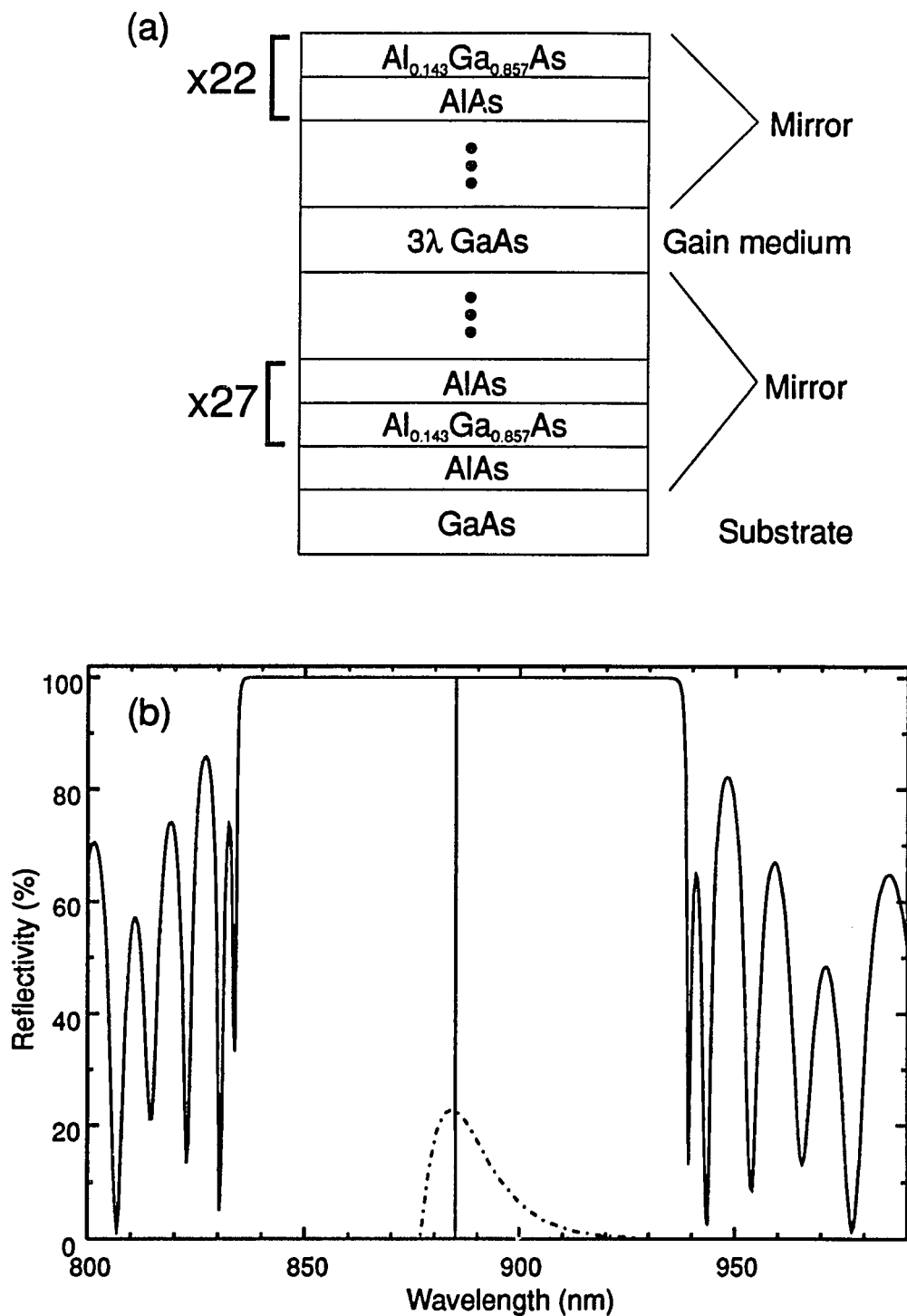


Fig. I.1 (a) Schematic of 3λ VCSEL structure. (b) Calculated reflectivity curve for 3λ VCSEL with Fabry-Perot dip at $\lambda \sim 885$ nm (broken line shows typical GaAs gain spectrum).

at $\lambda \sim 885$ nm (corresponding to the wavelength of laser emission). Small size, low threshold (sub-milliamp threshold has been reported using a single quantum well gain medium, see Jewell et al. (1991) and references therein), simple processing, planar array fabrication, single longitudinal-mode, and circular beam profile are a few of the characteristics that make VCSEL's attractive for applications.

Several different experiments with VCSEL's are considered in what follows. In chapter one, we look at what happens when an external laser signal is injected into an above threshold VCSEL. Two regimes of interactions are distinguished with unique observed phenomena. Chapter two concerns measurement of some VCSEL parameters, in particular the linewidth enhancement factor, carrier density and carrier lifetime. Finally, in chapter three we consider the microcavity laser threshold transition both experimentally and theoretically as the spontaneous emission rate into nonlasing modes is reduced.

CHAPTER ONE

MICROCAVITY LASER WITH INJECTED SIGNAL

Microcavity lasers have many desirable characteristics, however with the optically pumped (dye laser pump) samples we used, pump power fluctuations caused large linewidth fluctuations which precluded us from pursuing our initial experimental goals of studying laser instabilities due to optical feedback. In an attempt to circumvent this problem, we were prompted to attempt injection locking the VCSEL to a frequency stabilized single frequency dye laser. This however proved interesting in its own right and led us on a new trek to understand the behavior of a microcavity laser with an external injected signal. The initially irksome power fluctuations fortuitously led to a fruitful area of investigation. The following sections of this chapter describe our results in this regard. Roughly speaking, the many intriguing phenomena observed experimentally can be divided into two regimes: 1) injection signal intensity less than the output power of the VCSEL, and 2) injection signal intensity much greater than the output power of the VCSEL. The former case leads to such effects as injection locking, enhanced relaxation oscillations, etc. The latter to asymmetric local gain modification, multiwave mixing, etc.

Instabilities with Weak Injected Signal

Introduction

The dynamics of coupled oscillators has been explored in many different systems and has a long history (see Sargent et al. (1974) p. 52). Coupled

oscillators in the optical wavelength regime have been investigated since the 1960's first in gas lasers and more recently in semiconductor lasers [Siegmán (1986), Lang (1982), Kobayashi (1991), Mogensen et al. (1985), Hui et al. (1991)]. To date, studies of weak external light injection into an above-threshold semiconductor laser have been limited to edge-emitting structures with many longitudinal modes. The microcavity laser, with cavity length on the order of the wavelength of emitted light, is designed to have a single longitudinal mode within the gain spectrum of the active semiconductor material. As such this type of laser can be designed to lase at a pre-determined wavelength with specific gain and index properties (in contrast to ordinary edge emitters that lase at the wavelength of the gain curve peak). Here we study the effect of injecting a weak external laser signal into a single-longitudinal-mode microcavity laser near the free-running lasing frequency [Boggavarapu et al. (1993)]. Unique features appear experimentally in the nonlinear dynamics of this system including new frequency generation, subharmonic bifurcation, injection locking, and enhanced relaxation oscillations. The laser with injected signal is treated theoretically via laser rate equations.

Experimental Method

The GaAs/AlGaAs microcavity laser used in our experiments is grown by molecular beam epitaxy using a Riber 32P machine on a GaAs substrate. The top and bottom cavity mirrors consist of 22 and 27.5 periods of 625 Å Al_{0.143}Ga_{0.857}As / 733 Å AlAs, respectively. Designed reflectivities near the lasing wavelength are 0.9990 for the top mirror and 0.9995 for the bottom mirror. The 3λ active region (where λ is the emission wavelength) physically consists of 7357 Å of bulk GaAs.

Sample nonuniformity on a microscopic scale (on the order of microns) was a major impediment to performing experiments. An image of the sample of several micron spot size scanned across the sample revealed islands of growth and large variations in luminescence intensity (a similar problem is discussed by Oudar et al. (1992)). Lasing spots were few and far between. To tackle this problem, a few centimeter square portion of the unprocessed wafer was mounted on a temperature controlled thermoelectric (TE) cooler. In order to find lasing spots the entire TE cooled mount with wafer was translated using a precision Oriel motorized stage allowing micron resolution. Even with this capability, many hours were usually required to find a suitable lasing spot. Thermal drift of mounts and optical components required tweaking the setup at regular intervals during the day.

As stated above the samples were pumped optically to achieve lasing. This was the one major area of trouble that led to most of the investigations detailed here. Initial VCSEL samples while suffering from local nonuniformity (as mentioned above) also were grown with lower reflectivity mirrors than the ~ 0.997 mentioned above and with the Fabry-Perot peak shifted to shorter wavelengths requiring higher carrier density (and corresponding pump power) to extend the gain region to these higher energies. Thus lasing threshold was on the order of ~ 60 - 70 mW optical pump power. After initial success in achieving VCSEL lasing using a Coherent 699-21 dye laser pump, we proceeded to begin feedback instability experiments. The VCSEL linewidth was measured to be quite broad (several tens of GHz). It was found that pump power fluctuations of 2-3% caused large VCSEL linewidth jitter (pump fluctuation effect on linewidth is discussed by Agrawal et al. (1988a)), due to the nonzero alpha parameter of

the semiconductor medium (see chapter two). This prompted the high injection regime of experiments discussed in the next section of this chapter. To understand the high injection regime better, the low injection regime and the linewidth problem needed to be cleared up. The solution came in two parts as the next growth cycle of VCSEL samples exhibited significantly lower threshold (less than 10 mW at some spots) but still suffered from sample nonuniformity. This low threshold power allowed us to use a commercial high-power laser diode as the pump source (Spectra-Diode Labs model 5311-G1, output power $P \sim 100 \text{ mW}$). Luckily the lasing wavelength of the pump diode ($\lambda \sim 827 \text{ nm}$) corresponded to the first dip in reflectivity at the edge of the high reflectivity band of the top mirror of the VCSEL. Commercially available precision current controllers provide an extremely stable current source (nanoamp noise when producing $i \sim 100 \text{ mA}$ current) which translates to an extremely intensity-stable light source. Thus the stable optical pump leads to stable VCSEL intensity output and narrow frequency spectra.

Optical pump power was focused onto the VCSEL by an anti-reflection coated diode laser lens with a spot size of approximately $5 \mu\text{m}$ diameter. The pump laser diode was operated at a fixed current ($i \sim 116 \text{ mA}$) and temperature ($T \sim 14.9 \text{ C}$) by precision controllers manufactured by ILX Lightwave. Pump power to the VCSEL was controlled by adjusting the voltage applied to an acousto-optic modulator placed in the pump beam path. Lasing threshold was achieved with approximately 6.5 mW of pump power, and the lasing wavelength was $\sim 885 \text{ nm}$. Experiments were carried out at $\sim 8 \text{ mW}$ pump power with free running VCSEL lasing output power of $\sim 40 \mu\text{W}$. A reflection geometry was used in the experiments (to provide adequate heat sinking through the

substrate side) so that the lasing output of the VCSEL was collected via the same lens used to focus the pump light. The pump light and VCSEL output were spectrally separated by using a dichroic beamsplitter (high reflectivity at ~885 nm and high transmission at ~830 nm) and narrow bandwidth high contrast interference filter (center wavelength 880 nm). The subsequent VCSEL output light was divided with portions directed to a video camera, a 1.2m spectrometer (Spex Corp., resolution $< 0.1 \text{ \AA}$), and a Burleigh Corp. scanning Fabry-Perot interferometer (free spectral range~30 GHz, finesse~47). The external injection laser signal was provided by an argon pumped standing wave CW dye laser (Coherent model 599) with intracavity etalons (in order to operate single frequency) and was introduced to the VCSEL via a beamsplitter in the output light path. The complete experimental setup is shown in Fig. 1.1. Spatial overlap of the injection signal and VCSEL lasing mode was critical. Coarse frequency adjustments of the VCSEL and injection signal are monitored with the spectrometer; final adjustments are made by viewing the Fabry-Perot interferometer spectral trace.

Results

Experimental data were taken at several different positive and negative frequency detunings $\Delta \equiv \nu_{\text{vcsel}} - \nu_{\text{inj}}$. With injection signal detuned slightly positive ($\Delta = 5.1 \text{ GHz}$) we observe a sequence of frequency spectra shown in Fig. 1.2a as injection intensity is increased. Low injection levels result in a system where the two oscillation frequencies still compete. As the injection level is increased the original VCSEL frequency is suppressed and a ripple of sidebands appears on one side as in the third trace of Fig. 1.2a. Slightly higher injection levels result in complete frequency locking of the VCSEL to injected signal and

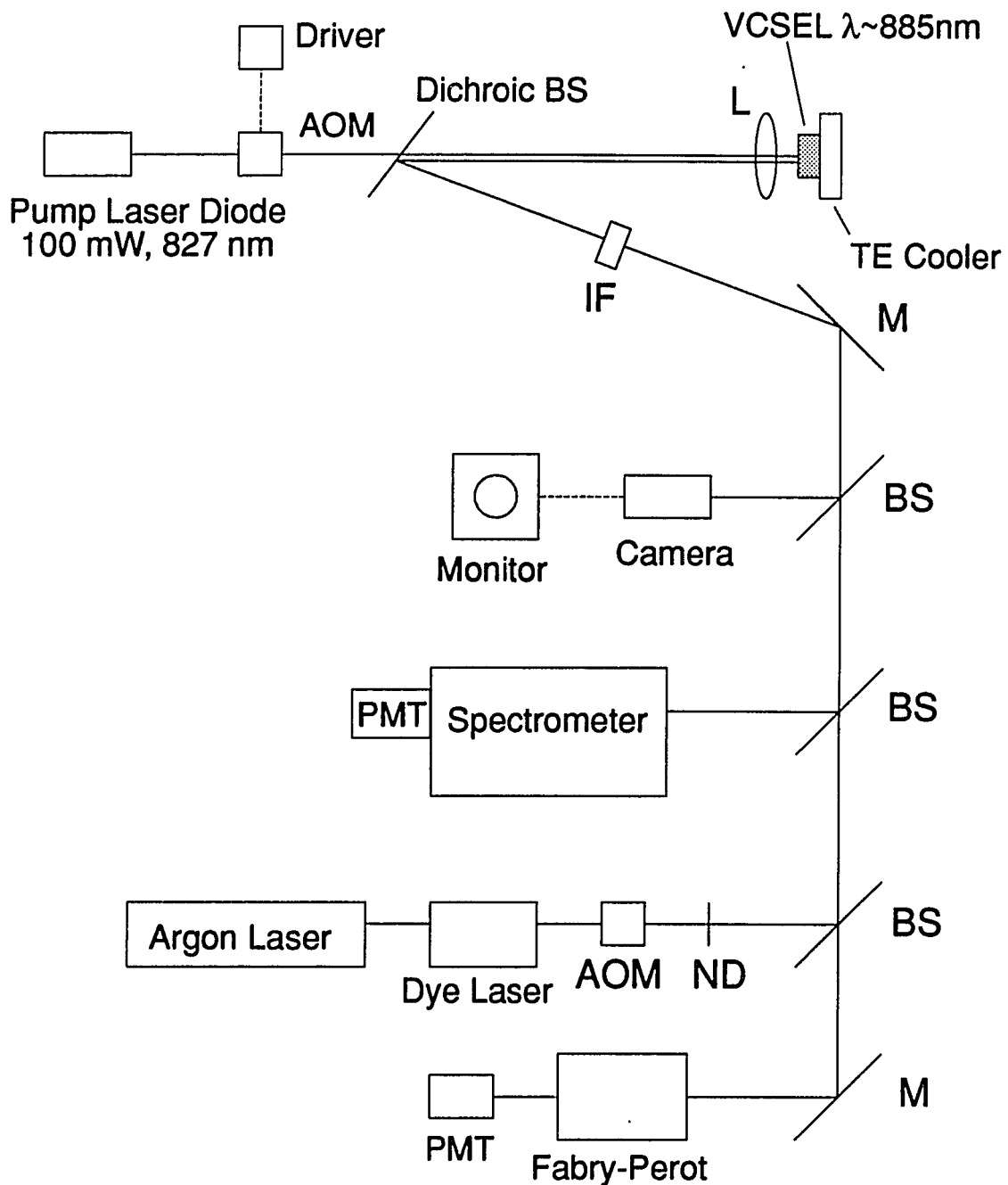


Fig. 1.1 Experimental setup to investigate injection dynamics. M-mirror; BS-beamsplitter; L-lens; AOM- acousto-optic modulator; PMT-photomultiplier tube; IF-interference filter; ND-neutral density filter; TE- thermo-electric.

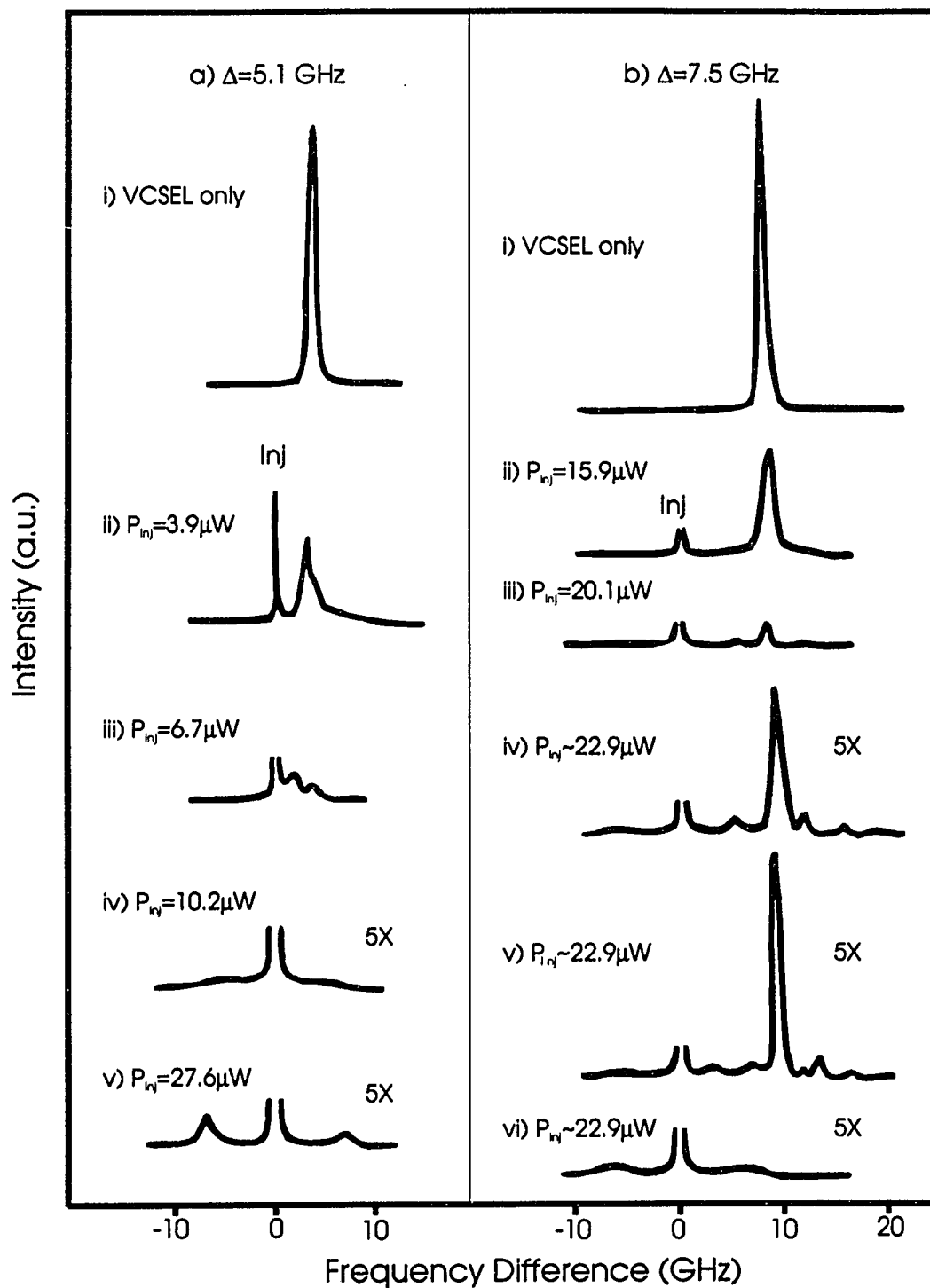


Fig. 1.2 Sequence of frequency spectra as injection intensity is increased for positive detunings (a) $\Delta = 5.1$ GHz and (b) $\Delta = 7.5$ GHz.

then the appearance of sidebands, as shown in the fourth and fifth trace of Fig. 1.2a. These sidebands are interpreted to be injection-enhanced relaxation oscillations. Note that locking occurs with injected signal of $\sim 10 \mu\text{W}$. Slightly larger positive detuning of injection signal ($\Delta=7.5 \text{ GHz}$) produces a sequence such as shown in Fig 1.2b. Now slightly more than twice the injection power of the previous case is needed for locking (final trace of Fig. 1.2b, $P_{inj}\sim 22.9\mu\text{W}$) with different dynamics prior to locking. In this case one-sided ripple sidebands do not appear but the VCSEL frequency strength is reduced as injection is increased as in the first three traces of Fig. 1.2b. The next three traces show the edge of an unstable regime of operation for this system wherein small noise fluctuations ($\sim 2\%$) in injected power result in the system going in (trace vi) and out (trace iv and v) of locking. This unstable regime also exhibits unusual behavior of new frequency generation at $\Delta/2$ (trace iv) and $\Delta/3$ (trace v) indicative of a bifurcation sequence. For larger positive detuning Δ , more power is required for injection locking until eventually the VCSEL is unable to frequency lock.

Negative frequency detunings (i.e. $\nu_{vcSEL} < \nu_{inj}$) were also investigated to ascertain if any asymmetric behavior existed. At small detunings the route to injection locking is shown in Fig. 1.3a ($\Delta=-3.5 \text{ GHz}$), which is very similar to that shown in Fig. 1.2a but in mirror image since the injection is now on the higher frequency side of the VCSEL. However at larger negative detuning, the dynamics change considerably from the case of similar positive detuning as shown in Fig. 1.3b for $\Delta=-8.5 \text{ GHz}$. Here the VCSEL does not lock at any injection power level (even when injection power is greater than the VCSEL output); rather the VCSEL frequency shifts away from the injection with

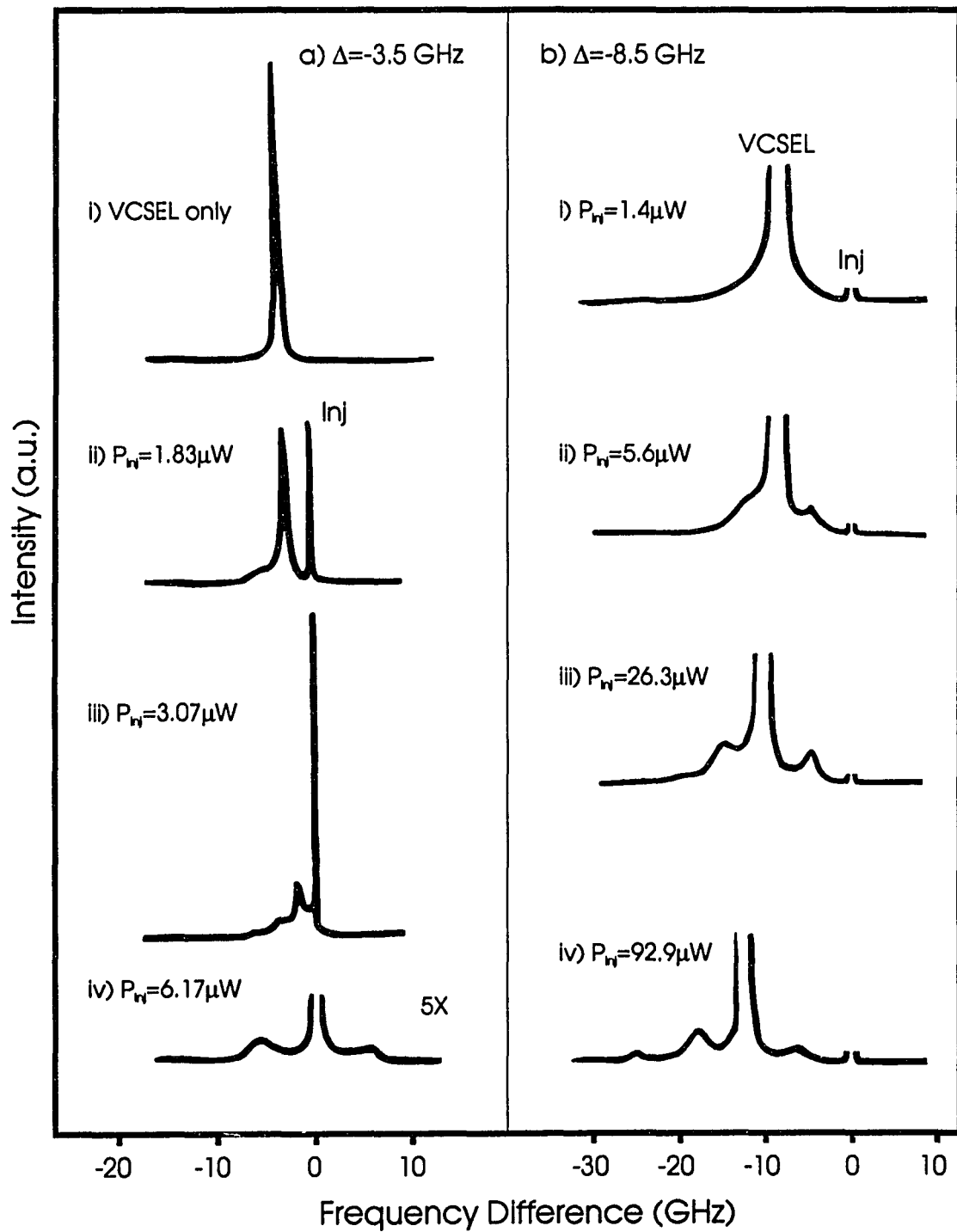


Fig. 1.3 Sequence of frequency spectra as injection intensity is increased for negative detunings (a) $\Delta = -3.5$ GHz and (b) $\Delta = -8.5$ GHz.

increasing injection. Also a new frequency is generated at half the injection-VCSEL frequency splitting in each trace of Fig. 1.3b.

Asymmetry in the range of frequency detunings over which locking occurs was first noticed by Lang (1982). This effect is unique to semiconductor lasers and is explicitly caused by the fact that the real and imaginary parts of the dielectric susceptibility are coupled for this medium (i.e. the alpha parameter - see chapter two). Figure 1.4 shows the experimental data points for reciprocal locking power (i.e. zero power means the VCSEL does not lock to the injection) as a function of frequency detuning with the asymmetry clearly apparent. This point will be returned to in chapter two in the discussion of the linewidth enhancement factor.

Theoretical Model

We now turn to provide a theoretical basis for understanding the experimentally observed phenomena (modeling was done in collaboration with the group of S. W. Koch and carried out by Y. Z. Hu). In analogy to the development of Spencer and Lamb (1972), the laser with injection can be described by standard coupled rate equations for the total field amplitude E , field phase ϕ , and carrier density N . To properly treat the semiconductor case, the nonzero α -parameter (see chapter two) must be included. The injection signal is assumed to be weak, allowing the equations to be linearized about the zero injection VCSEL lasing solution, yielding

$$\frac{dE}{dt} = \Delta N \frac{dg}{dN} E + \frac{c}{2Ln} t_r E_i \cos \phi \quad (1.1)$$

$$\frac{d\phi}{dt} = \Delta + \alpha \frac{dg}{dN} \Delta N - \frac{c}{2Ln} t_r \frac{E_i}{E_0} \sin \phi \quad (1.2)$$

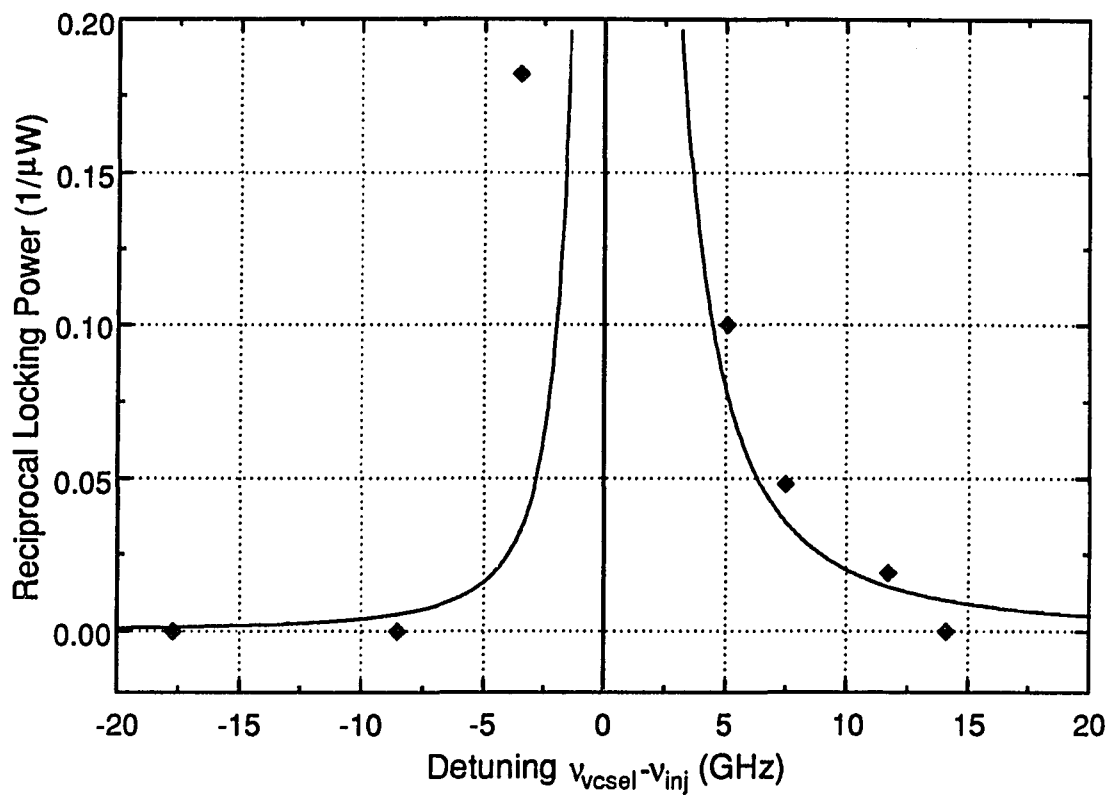


Fig. 1.4 Reciprocal of the injection power level needed to frequency lock the VCSEL as a function of detuning. Note the asymmetry for positive and negative detunings. The solid line shows the functional form of the asymmetry assuming $\alpha=2.0$.

$$\frac{d\Delta N}{dt} = k_n g(N_{th}) E_0^2 - \gamma \Delta N - k_n g(N) E^2 \quad (1.3)$$

where $g(N) = dg/dN \cdot \Delta N$ is carrier density dependent gain, $\Delta N = N - N_{th}$ is carrier density deviation from threshold, E_0 is VCSEL field without injection, E_i is injected field strength outside the cavity, t_r is the VCSEL mirror transmission, γ is the carrier decay rate, L is cavity length, n is background index, α is linewidth enhancement factor, Δ is frequency detuning, and constants are grouped into $k_n = n^2 \epsilon_0 / h\nu$. The phase ϕ is defined as the difference in phases between the injection field and VCSEL field. The many body theory of semiconductor band edge nonlinearities [Haug et al. (1990)] is used to calculate $dg/dN = 1.57 \times 10^{-7} \text{ cm}^3/\text{sec}$ and $N_{th} \sim 1.1 \times 10^{18} \text{ cm}^{-3}$. The parameters used in our simulations are $L = 1 \text{ }\mu\text{m}$, $n = 3.5$, and $t_r = 0.003$, $1/\gamma = 1 \text{ nsec}$, $g(N_{th}) = 2.57 \times 10^{11} \text{ sec}^{-1}$, $\alpha = 2.0$, and $E_0 = 20.1 \text{ kV/cm}$ (corresponding to relaxation oscillation frequency $f_{ro}^2 = (I_0 n g(N_{th}) dg/dN) / (\pi^2 h \nu c) = (2 \text{ GHz})^2$, with $I_0 = n \epsilon_0 c E_0^2 / 2$). Note that the injected signal is assumed to be a weak perturbation (i.e. $P_{inj} \ll P_{vcSEL}$) in deriving these equations, and as such this model cannot be used to simulate situations where a strong external injection signal is used. The rate equations (1)-(3) were integrated in time using the fourth order Runge-Kutta method. Time series data were Fourier transformed to obtain frequency spectra plots to compare with experiment. Typical computed frequency spectra are shown in Fig. 1.5 as injection intensity is increased down the column (the injection is shown in the center of each figure), along with the computed phase portrait of the complex electric field. The behavior seen here is similar to that experimentally observed in Fig 1.3b where the VCSEL does not lock to the injection but instead shifts and develops new frequencies.

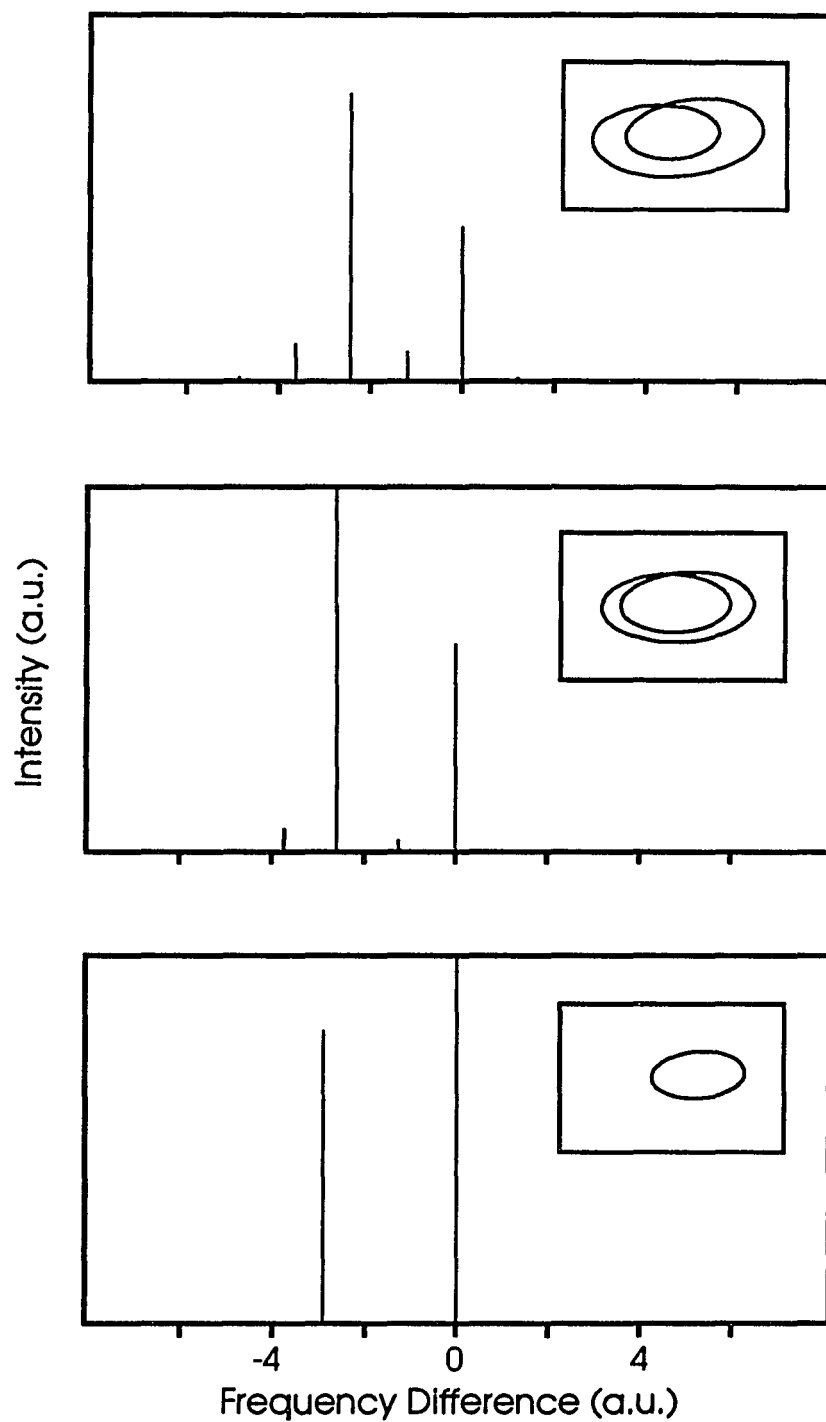


Fig. 1.5 Theoretically computed frequency spectra for increasing injection (injection is located at zero detuning). The inset shows the phase portrait of the complex electric field.

Summary

The laser with injected signal provides a unique system to study nonlinear dynamics of coupled oscillators, and now with the advent of the microcavity laser, dynamical studies in the smallest of laser cavities is possible. By investigating different cases of frequency detuning and injection power level, unusually rich behavior is observed. These include new frequency sideband generation, subharmonic frequencies, injection locking and enhanced relaxation oscillation sidebands. Numerical simulations based on a model of coupled rate equations for the field amplitude, field phase, and carrier density yield good agreement between theoretical and experimental trends.

Asymmetric Local Gain Modification

Introduction

In the previous section we discussed weak optical injection. We continue along this path, the road less traveled now, and consider strong optical injection (i.e. injection signal greater than VCSEL laser power). This is an intriguing regime not extensively studied as this is not normally thought of as practical (e.g. frequency locking, etc.). The initial impetus for studying this regime of operation, as described above, was to look for injection locking. However, as seen in the previous section, injection locking occurs at low injection power levels. After obtaining a few interesting experimental results in the high injection regime, it was realized that local gain modification was a plausible explanation, in analogy to Raman and Rayleigh gain in atomic systems [Mollow (1969), Wu et al. (1977), Haroche et al. (1972), Khitrova et al. (1988a), Grantham (1991)]. Specifically, experimental evidence pointed to enhanced gain on the low energy

side of the strong injection signal and suppressed gain on the high energy side. Several recent theoretical papers [Sargent et al. (1988), Lindberg et al. (1989), Zhou et al. (1990), Paul et al. (1990)] developing these Mollow-spectrum type effects taking into full account semiconductor band structure and many body effects provided added reason to continue this line of investigation (although calculations did not give exact numerical agreement with experiment). In the following we present the experimental evidence for asymmetric gain modification first along with some qualitative arguments. We then discuss some background and the physical processes responsible for local gain modification in semiconductors.

Experimental Method

Experiments were carried out with two different VCSEL samples with different operating conditions and different sources of optical pump power. The first series of experiments was done with a dye-laser optical pump source. A second series of experiments was done using a diode laser pump source in order to clarify data of the first experiment. This second experimental setup was exactly as described in the previous section (with the same sample) except with higher injection power levels. We briefly describe the sample and setup of the first experiment. The VCSEL consisted of a 17 period top mirror of alternating quarterwave layers ($619 \text{ \AA} \text{ Al}_{0.127}\text{Ga}_{0.873}\text{As} / 732 \text{ \AA} \text{ AlAs}$), 3λ optical thickness bulk GaAs active region, and 22.5 period bottom mirror of the same material as the top mirror. In this case the mirror reflectivities were lower than those of the sample previously described resulting in a single Fabry Perot peak width of $\sim 5 \text{ \AA}$. A wedge in growth thickness across the wafer led to lasing wavelength variation from 873 nm to 881 nm at different spots. Typical threshold pump

power for CW lasing ranged around 65 mW necessitating use of a thermoelectric cooler to maintain sample temperature at approximately 10 °C. Experiments were carried out with pump power of approximately 270 mW.

The experimental setup, while providing the same functionality, was slightly different from previously described and is therefore briefly explained. Optical pump power to the sample at ~830nm wavelength was provided by an argon pumped ring dye laser (Coherent 699-21). The injection laser signal was provided by another argon pumped 699-21 ring dye laser, this time actively frequency stabilized to ~1 MHz RMS linewidth. This laser could be electronically scanned ± 15 GHz, while maintaining narrow linewidth, and also manually tuned over a range of ~3 Å with an intracavity etalon. An acousto-optic modulator was placed in each dye laser path to prevent deleterious feedback effects. Spectral data were obtained with the same scanning Fabry Perot interferometer and 1.26m spectrometer with photon counting apparatus mentioned previously. The Fabry Perot was adjusted to have a free spectral range of 157.5 GHz (finesse ~47) to study the wider frequency range allowed by the broader Fabry Perot peak of this VCSEL sample. As mentioned, amplitude noise in the pump dye laser caused large linewidth fluctuations in the VCSEL laser linewidth, necessitating quick data acquisition. The Fabry Perot scan rate was adjusted to maintain signal integrity and minimize acquisition time. Data acquisition with the spectrometer in conventional scan mode was quite slow (several minutes), which hurt signal to noise ratio. This problem was overcome by using the spectrometer in a continuous scan mode, and by using the two registers of the photon counter in a synchronous mode with an optical chopper allowing simultaneous acquisition of data and background all in less than one

minute. Significant improvement in signal to noise ratio and reproducibility were immediately discernible (though these spectra were still muddy compared to those obtained with the diode laser pumping).

Experimental Evidence

First hints of unique behavior were provided by the appearance of new sidebands appearing around the injection signal as shown in the Fabry Perot trace of Fig. 1.6. Especially intriguing here is the extinction of the initially broad VCSEL lasing line by the strong injection and the appearance of sidebands (panels (b)-(d)) which move away from the injection with increasing injection power. The sideband labeled I_3 appears first and I_4 is the result of wave mixing of I_3 with the injection ($\nu_4=2\nu_{inj}-\nu_3$). A second order mixing signal is seen on the low frequency side of I_3 in Fig. 1.6c ($\nu=2\nu_3-\nu_{inj}$). The intensity dependent sideband frequency splitting is found to scale as the square root of the injected power, with splittings up to 48 GHz. This caused initial excitement as the square root dependence of sideband splitting is well known in regard to driven atomic systems with Raman gain (subsequent experiments inspired by this work showed $\Delta \sim \sqrt{P_{input\ injection}}$ or $\Delta \sim P_{intracavity\ injection}$ in agreement with theory, see Lowry et al. (1993)). Further reading revealed that this square root intensity dependence also arises in determining the relaxation oscillation frequency of laser diodes, however the frequencies observed here are much larger than usual observed relaxation oscillation frequencies [Yariv (1989)]. This caused some confusion and caused us to look at ways to clarify the origin of the sidebands. The broad VCSEL laser linewidth obscured the initial growth and appearance of the sidebands at low injection levels, a point clarified below when we discuss the second set of experiments done with a higher quality VCSEL sample.

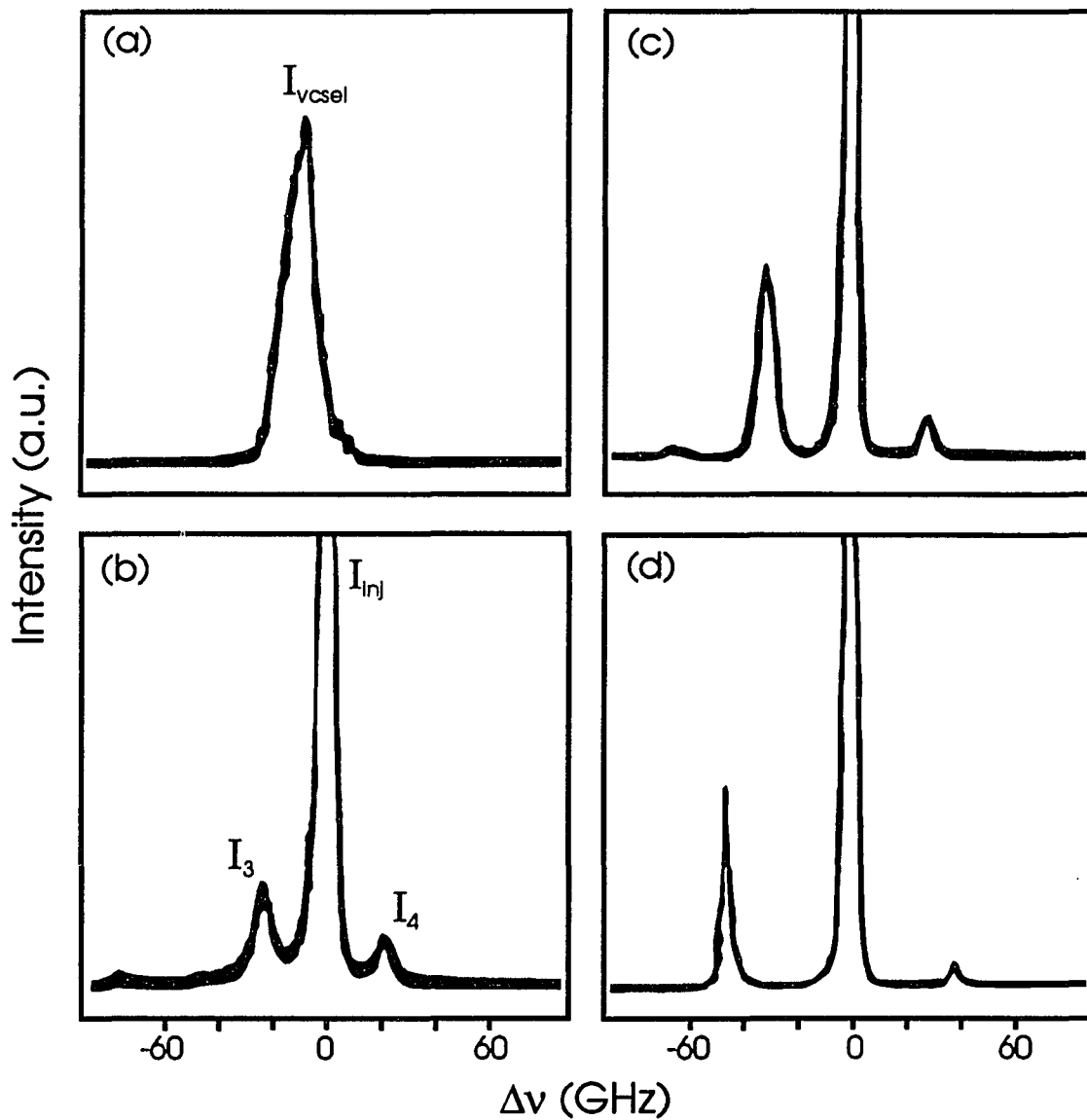


Fig. 1.6 Unmodified and modified frequency spectra of the VCSEL lasing. (a) VCSEL lasing without injection, peak at 874.5 nm with output power of 0.1 mW. (b)-(d) VCSEL output with injection at a frequency slightly above ν_{vcse1} and with power (mW) of (b) 0.23, (c) 1.2, (d) 2.5. (c) and (d) have the same vertical scale; relatively (b) scale has been magnified by a factor of 2. For comparison I_3 in (c) is 0.056 mW.

To obtain further complementary information about asymmetric gain modification, we studied various cases of VCSEL - injection frequency detuning as a function of increasing injection power. One case of particular significance is shown in Fig. 1.7. In this sequence, taken as a function of increasing injection, one sees the original VCSEL lasing pushed away from the injection signal (to higher energy) and simultaneously extinguished. At the same time one notices the appearance of a small new sideband on the low energy side of the injection that moves out with increasing injection level. The extinguishing of the VCSEL signal is interpreted as the development of a local hole in the gain curve on the high energy side of injection and the concurrent formation of enhanced gain on the low energy side leading to the sideband I_3 . One worry in interpreting the data was the possibility of the injection signal causing an overall reduction in carrier density, thereby causing a decrease in the nonlinear index of the active medium, resulting in a redshift of the cavity Fabry Perot peak. Curves shown in Fig. 1.7 serve to dispel this possibility since the VCSEL signal is pushed to shorter wavelengths while a carrier density reduction would cause a shift of the VCSEL to longer wavelengths. It is clear that something other than overall carrier density reduction must be occurring.

Up to this stage in our research, the evidence for asymmetric gain modification was only through indirect deduction. To try to get some feel for the actual shape of the local gain modification, we performed another run similar to that above but processed the data differently. Shown in Fig. 1.8a by the dotted line is the broad original VCSEL lasing line. Superposed on this is the spectrum modified by the injection signal. We now take the natural logarithm of the ratio of the injection modified curve divided by the original VCSEL line with the

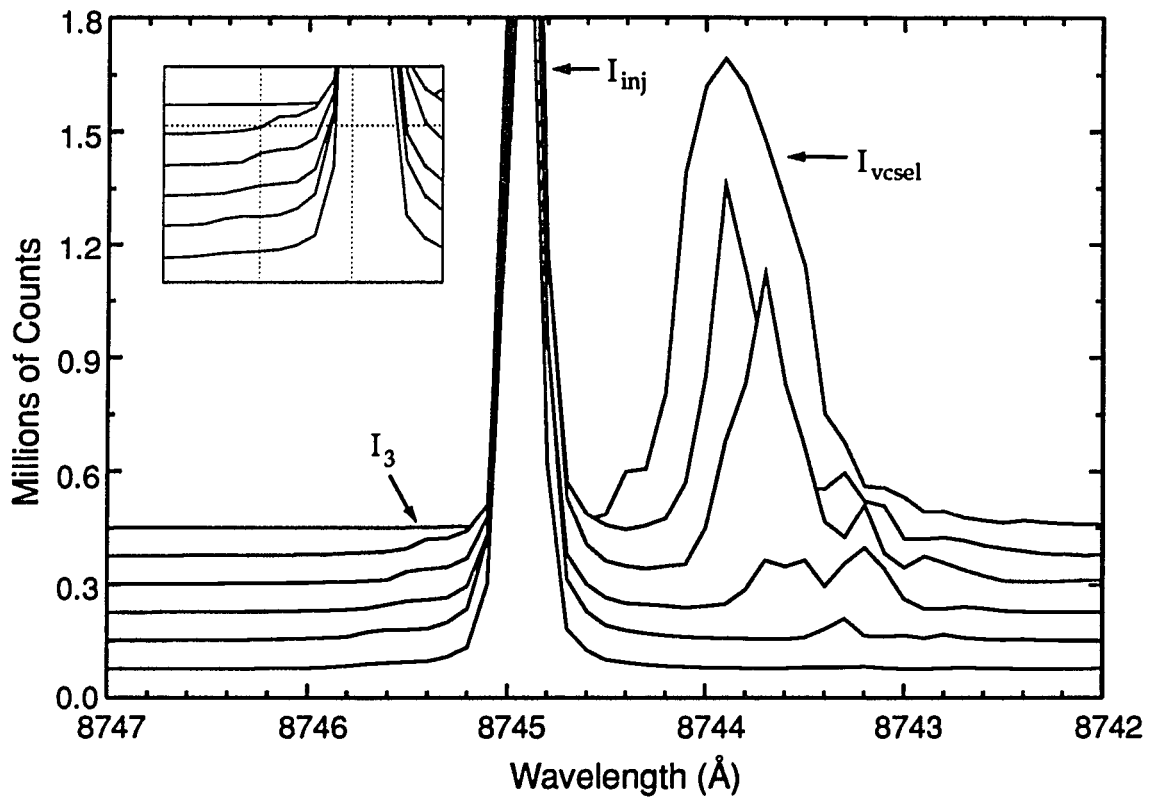


Fig. 1.7 Evidence for asymmetric gain modification. Graphs are VCSEL output spectra with increasing injection intensity (curves are offset for clarity). The injection is at 8744.9 Å with $P_{inj}=0.0, 0.59, 0.76, 1.4, 2.5, 2.8$ mW (top to bottom). VCSEL lasing without injection: $P_{vcse1}=0.18$ mW, peak at 8743.9 Å, 58:1 vertical to horizontal polarization ratio.

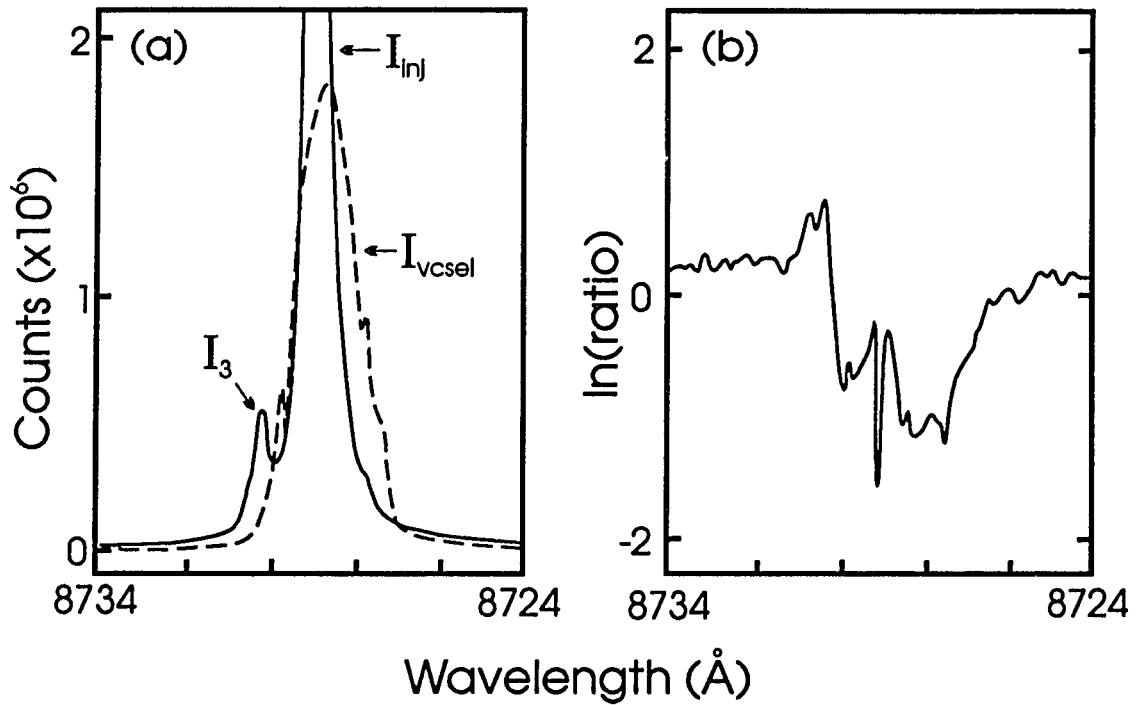


Fig. 1.8 Shape of the asymmetric gain modification. (a) Spectra of the VCSEL lasing without injection (dashed curve; $P \sim 0.48$ mW) and with 2.9 mW injection (solid curve). (b) Natural logarithm of the ratio of the above graphs showing the asymmetric gain modification; imperfect subtraction of the injection results in the M-shaped feature at 8728.8 Å. The narrowness of the Fabry Perot prevents seeing gain changes outside the ~ 4 Å bandpass.

result shown in Fig. 1.8b (we subtract out the injection signal as well as possible before taking the ratio but a small M-shaped canyon artifact of injection remains at $\sim 8728.8 \text{ \AA}$). The purpose of this processing is to obtain a differential spectrum revealing the effect of injection, something like $\Delta\alpha(\nu)$. Clearly present here is the gain enhancement at wavelengths longer than the injection and the gain dip on the opposite side of the injection. One question that arises is whether the injection creates local holes in the electron and hole distributions which modifies photoluminescence emission. Electron and hole distributions equilibrate to Fermi-Dirac functions on the time scale of the carrier-carrier scattering time of the medium ($\tau_{cc} \sim 50\text{-}100 \text{ fsec}$, calculated by Binder et al. (1992)). The reciprocal of frequencies considered here ($>$ tens of picoseconds) is long compared to τ_{cc} which precludes the formation of local holes in carrier distribution (also coherent effects can be neglected as the Rabi frequencies, even with injection, are small compared to $1/\tau_{cc}$). Another doubt could arise from overall carrier density reduction arguments. If indeed the carrier density were reduced in the active region causing a redshift of the Fabry Perot peak, one would expect the signal to be enhanced at longer wavelengths in the numerator precisely where the denominator would have smaller signal, resulting in a curve similar to Fig 1.8b. But as mentioned in the last paragraph, strong arguments against Fabry Perot shift could be presented from data in Fig. 1.7, which adds credence to the evidence offered in Fig. 1.8b. Note that although Fig. 1.8b is dispersive-like in shape its zero crossing is not at the injection wavelength, a feature also apparent in theoretically calculated curves (see Fig. 1.12).

Data presented to this point were obtained with the broad VCSEL lasing line of a dye-laser-pumped sample, clouding the origin of the newly generated

frequency and the nature of injection locking. By going to a higher quality sample and diode laser pumping, a fog was lifted and details heretofore unbeknownst to us beckoned further investigation. The route to injection locking became clear as the starlit night sky. The argument concerning relaxation oscillations as the origin of the new frequency could then be laid to rest, as both theory and experiment showed relaxation oscillation sidebands (see Fig. 1.2a trace v) to be spaced less than 10 GHz from the injection signal (Lin et al. (1992) showed relaxation oscillation frequency up to 39 GHz for a highly excited VCSEL in a transient experiment; our excitation level was far less than theirs implying a much smaller relaxation oscillation frequency). To obtain clear data in the high injection regime, we used the exact same procedure of the previous section, merely increasing the injection level by rotating a neutral density filter wheel.

One sequence of high injection data is presented in Fig. 1.9 for an initial VCSEL-injection detuning of $\Delta=5.1$ GHz. These data are all taken after injection locking has already occurred at much lower injection levels. In the lowest injection level trace shown here (0.16 mW), injection-enhanced relaxation oscillation sidebands are clearly visible with a second order sideband also visible. As the injection level is increased the sidebands decrease in strength and move in towards the injection signal with asymmetric frequency splittings (compare, for example, the 0.16 mW and 0.36 mW trace in Fig. 1.9), contrary to what one might expect. An especially strong asymmetry between positive and negative detuning is apparent. For example, the positive frequency sidebands are not even visible at an injection level of 0.70 mW whereas the negative frequency sidebands are still pronounced. It is the step from this trace to the next

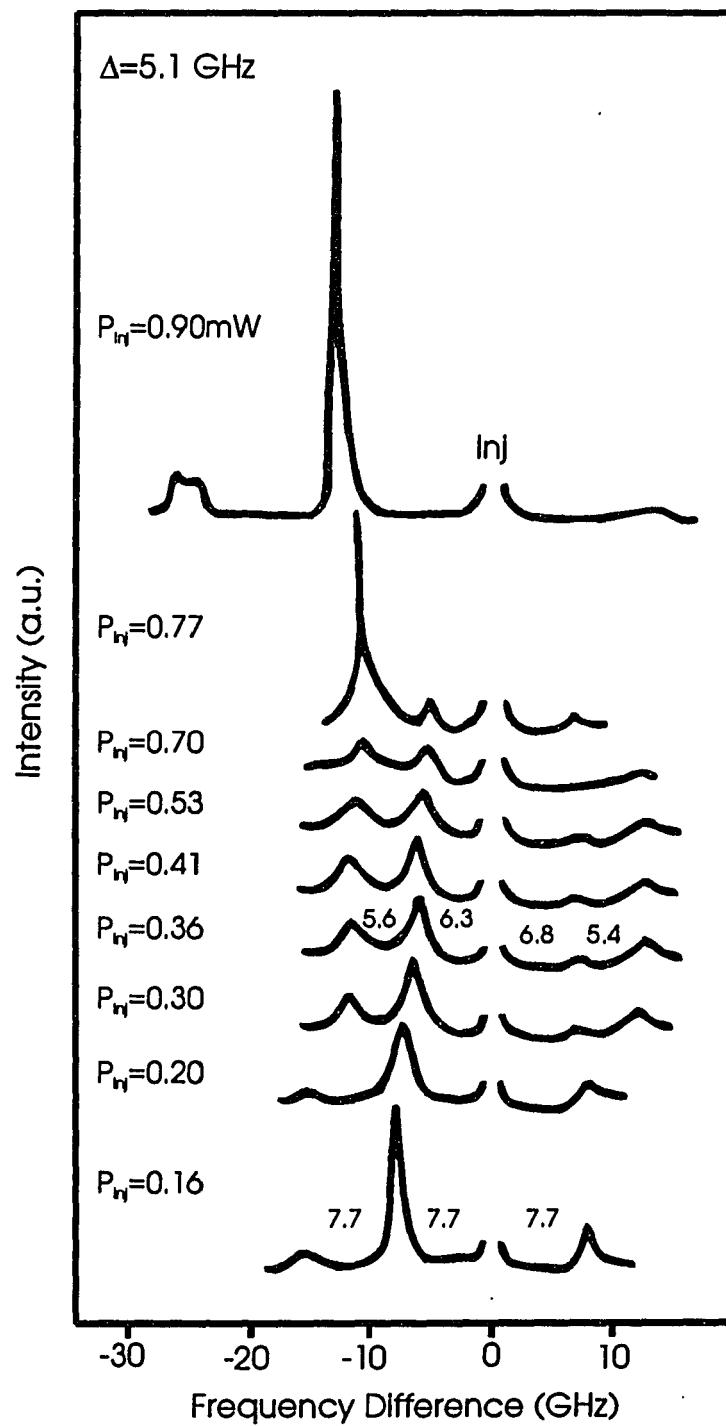


Fig. 1.9 Sequence of frequency spectra for high injection with original detuning $\Delta = \nu_{vcsel} - \nu_{inj} = 5.1$ GHz (all injection powers in mW). The numbers in the 0.16 and 0.36 mW traces indicate frequency splittings of adjacent bumps (GHz).

higher injection level that shows the birth of the strong new frequency, corresponding to that observed in Fig. 1.6. Increasing the injection level causes the new frequency to grow stronger (final trace, Fig. 1.9), and shift frequency as shown in Fig. 1.10 (approximate square root dependence on P_{inj}).

The jump apparent in the 0.77 mW trace of Fig. 1.9 is very reminiscent of the pronounced transition one sees at threshold in any laser and as such raises the question of whether this new frequency may actually be considered to be lasing. One plausible argument is that the enhanced gain at frequencies below the injection grows as the injection level is increased until the locally modified gain reaches the loss line allowing the new frequency to lase (lasing due to coherent energy transfer, without inversion, has been seen in sodium vapor by Khitrova et al. (1988b)). The intensity dependent frequency shift could then be explained by the shift of the locally modified gain peak with increasing injection. Support for lasing is provided by the spectrum shown in Fig. 1.11. Here we show the newly generated frequency in blowup with two small bumps symmetrically spaced around the base (this spectrum was taken with initial VCSEL-injection detuning of $\Delta=11.7$ GHz; evolution to new frequency generation following low power injection locking is similar to that of Fig. 1.9). These bumps are of reasonable size and frequency spacing (~ 2 GHz) to be relaxation oscillation sidebands. Relaxation oscillations are indicative of lasing since they arise from competition between photon number and carrier density in responding to noise fluctuations while staying clamped at the loss line.

Discussion

Having presented experimental evidence in the last section, we discuss some past experimental work. A brief physical description of the theory follows

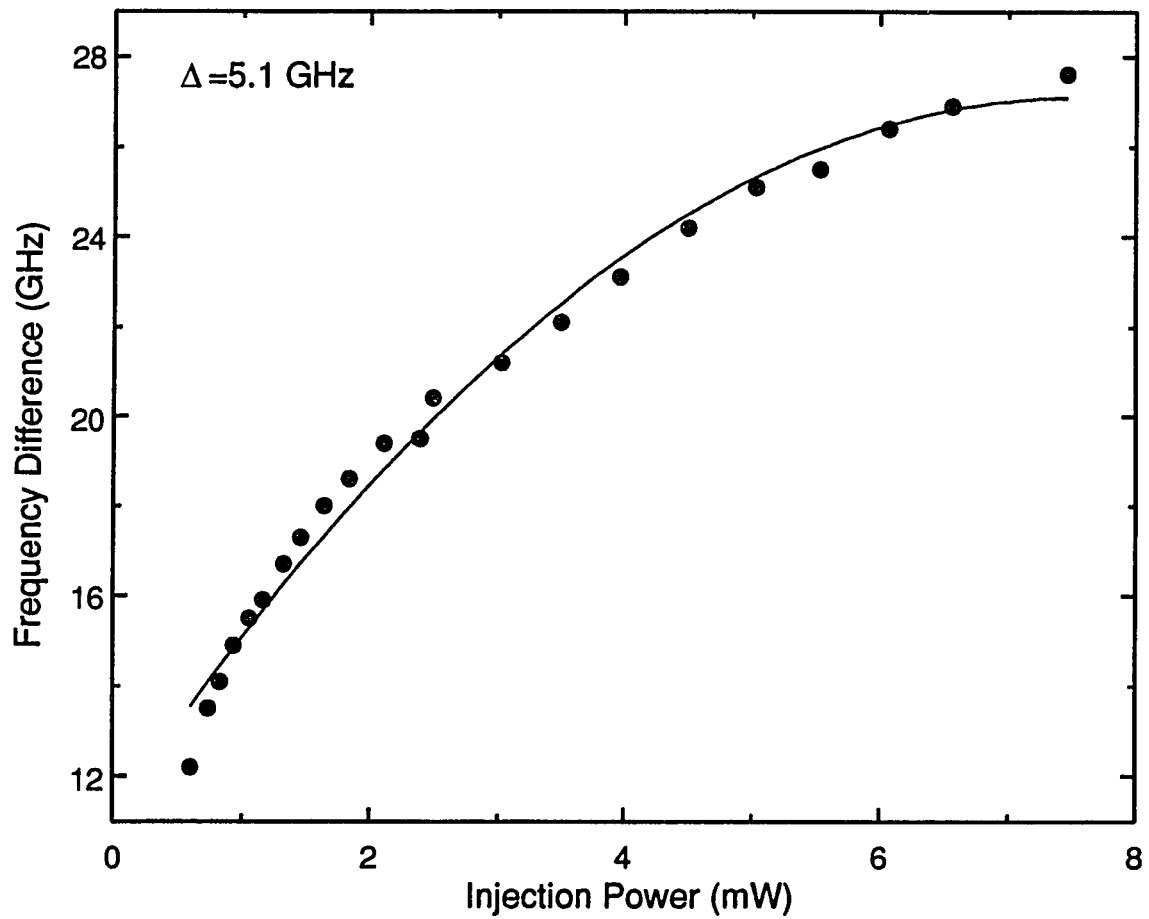


Fig. 1.10 Frequency difference between the newly generated signal (see previous figure) and injection as a function of injection power for initial detuning $\Delta=5.1$ GHz. The solid line is a quadratic fit to the data.

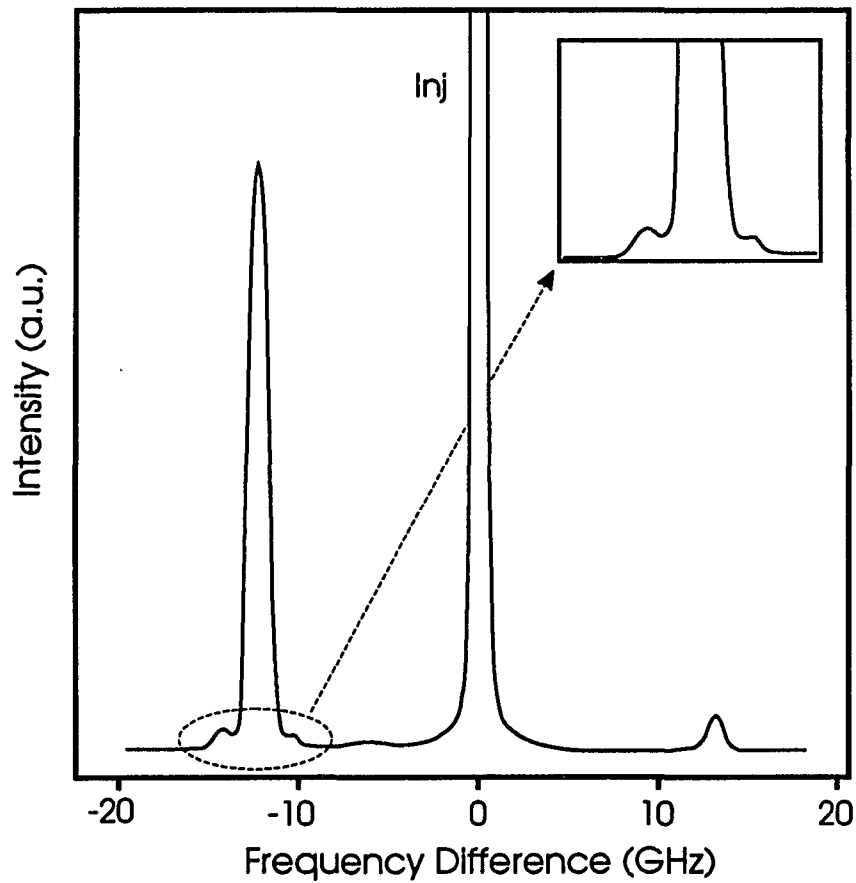


Fig. 1.11 Frequency spectrum with new signal generation at high injection ($\Delta = \nu_{\text{vcsel}} - \nu_{\text{inj}} = 11.7$ GHz, $P_{\text{inj}} = 0.97$ mW). Notice in particular the small relaxation oscillation bumps at the base indicative of lasing.

to put our experimental data in context. The first experimental hints of asymmetric gain modification were shown by Bogatov et al. (1975). They noticed asymmetry in the intensity of adjacent longitudinal modes of a conventional laser diode in an external cavity configuration. A model based on the beat frequency response of the total carrier density was presented to explain their data. A number of four wave mixing experiments conducted in the mid-80's using traveling wave semiconductor amplifiers (see Saitoh et al. (1991) and references therein) also showed evidence for local asymmetric gain modification. Again, due to small detunings of pump and probe (i.e. detunings less than $1/\tau_c$, where τ_c is the carrier lifetime), data could be explained by modulation of the total carrier density. Subsequent four wave mixing experiments in traveling wave amplifiers [Provost et al. (1989), Nietze et al. (1991), Tiemeijer (1991), Kikuchi et al. (1992)] showed asymmetry and beat signal generation at frequencies much larger than $1/\tau_c$ (up to 500 GHz) which required a new explanation. Earlier, it was proposed that such large beat frequencies should be observable due to modulation of intraband occupation probability without overall carrier density modulation [Agrawal (1988b)]. One final experiment of note was conducted by Chinn (1991) in which neighboring non-lasing longitudinal modes of a diode laser were used to deduce local gain modification caused by the single lasing mode. The shape of the asymmetric gain curve was shown to extend for up to several hundred GHz around the lasing mode, however the cavity mode spacing of 75 GHz allowed only a few data points and precluded any information on gain modification at small detunings. None of the experiments mentioned above investigated the intensity dependence of the gain modification.

To fully explain this phenomenon, we relate the ancient parable of Kilimanjaro, passed down through the centuries as a bedtime story. Two climbers taking a brief respite from ascending the heights of Kilimanjaro were approached by a hare who inquired, "*What's up doc? Dis dip on de right an dat riz on de left - it just dunt seem right, whaz happenin rastaman?*" The first climber, the ever prepared quintessential German physics professor (QGPP), delved into his rucksack, pulled out his latest scroll on the subject along with his expandable whiteboard and began to explain. Meanwhile the second climber, the down home country boy (DHCB), wandered off to find an appropriate location from which to convey his latest thoughts to his research clan via smoke signals (the fax machine was soon thereafter invented by a frustrated apprentice). The professor's original whiteboard with equations was thought to be lost (recently rediscovered in a major archeological find by Sargent et al. (1993) and references therein), and thus only an abridged version of his remarks remain (though it is claimed that the original dialogue can still be heard echoing through the mountain passes during monsoon storms):

We consider a multimode electric field with strong pump wave and weak signal and conjugate waves, where the field envelope is assumed to satisfy the slowly varying envelope approximation and rate equation approximation. The field induces a polarization in the medium proportional to the complex susceptibility. In the quasiequilibrium approximation, the susceptibility directly depends on carrier density and only indirectly depends on the multimode field envelope through the carrier density. We expand the carrier density in terms modulated at the beat frequency of the pump and signal wave. The modulation of the

carrier density is small, which allows us to expand the susceptibility in terms with the same beat frequency. We describe the dynamics of the medium by the equation of motion for the carrier density, which contains a term proportional to the square of the total electric field and the imaginary part of the susceptibility. The complicated many body effects of the medium (bandgap renormalization, Coulomb enhancement, etc.) are taken into account via the imaginary part of the complex susceptibility. Carrying out the algebraic manipulations and keeping only terms modulated at the beat frequency, we arrive at the coefficients appearing in the carrier density expansion. Substituting the carrier density expansion back into the susceptibility expansion and polarization finally leads to an equation for the signal wave polarization component of the medium. The solution to the slowly varying Maxwell equation, driven by the polarization, allows us to find the signal and conjugate wave coupling to the pump wave. Rapid carrier-carrier scattering in the semiconductor allows it to be treated as a homogeneously broadened medium, with power broadened decay rate proportional to light intensity, even though the large sum over k-states might imply inhomogeneous broadening. The large frequency splittings experimentally observed (compared to $1/\tau_c$) are explained by the fact that high light intensity inside the VCSEL increases stimulated processes (both absorption and emission) while having minimal effect on total carrier density. The asymmetric shape of the gain modification (see Fig. 1.12) is attributed to the rapid change of the electron Fermi-Dirac distribution function as a function of carrier density at the

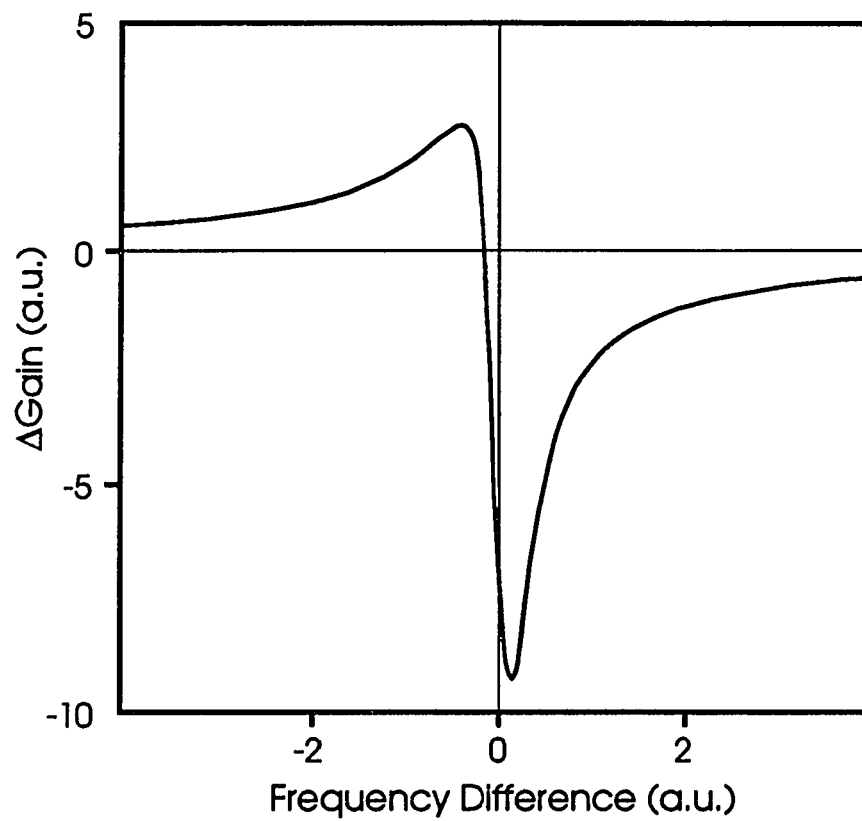


Fig. 1.12 Theoretically calculated curve of asymmetric local gain modification (from Sargent et al. (1993)). Notice that the zero-crossing does not lie at the pump frequency (zero frequency difference).

quasiequilibrium chemical potential (which lies above the gain region), preferentially weighting contributions above the gain region.

Having seen the board runneth over with equations, the hare recognized the professor's mathematical prowess and thanked him for his patience. The hare was cognizant of the importance of beating but remained unsatisfied, having lost most of the physics in the mathematical formalism. At this point the second climber returned and noticed the perplexed look on the hare's face. Realizing that the hare lacked a physical picture, the DHCB matter-of-factly stated, "*Elementary, my dear hare. Population Pulsations.*" Elated, the hare jumped up and danced a little Irish jig. The hare remembered the many long hours spent in school struggling through tedious mathematics to little avail, and finally understanding population pulsations, moving gratings, and the phase shift in the medium while watching the turquoise waters gently wash the rocky shores on the island of Favignana. Singing about how the off-resonance dipole response results in a $\pi/2$ phase shift yielding the dispersive like profile (or in other words, the induced index grating predominates over the gain grating), the DHCB joined in dancing the jig. The three travelers, having formed a common bond through physics, exchanged e-mail addresses, and submitted a NSF travel grant proposal to visit Kanchenjunga for continued future collaboration. Thus, one hare at a time, the progress of physics marches on.

Summary

Strong external light injection into the lasing peak of a VCSEL leads to local modification of the semiconductor gain curve and new frequency generation. The asymmetric shape of this local modification, with enhanced gain at energies below the injection and suppressed gain at energies above the

injection can be explained in term of coherent energy transfer from the strong injection light via population pulsations of the carrier density.

CHAPTER TWO

CHARACTERISTICS OF MICROCAVITY LASERS

Linewidth Enhancement Factor

Introduction

The ubiquitous semiconductor laser has evolved from being a pure research endeavor to wide commercial application due to its small size and low cost. However, all is still not understood about these lasers as they continue to reveal unique physics due to the complexity of the semiconductor medium. One of the most significant differences between the semiconductor medium and other gas or solid state laser media is the strong coupling of the real and imaginary parts of the dielectric susceptibility in a semiconductor. This characteristic of the medium manifests itself as a parameter known variously as the linewidth enhancement factor (LEF), linewidth broadening factor (LBF), α -parameter (alpha parameter), or antiguiding factor in semiconductor laser physics [Lax (1967), Haug et al. (1967), Henry (1982), Osinski et al. (1987)]. This parameter arises in almost any discussion of semiconductor laser properties and has as such become one of great importance in understanding semiconductor lasers. One effect of the LBF is to significantly broaden the linewidth of a semiconductor laser beyond the Schawlow-Townes limit.

Measurements of the LBF have to date all been done in edge-emitting laser cavity designs with cavity lengths of the order of one hundred to several hundred microns, with measured values ranging from 2 to 8 [Osinski et al. (1987)]. One reason for such a large discrepancy in the LBF value is that

measurements performed on long cavity lasers were invariably affected by waveguiding and possibly by multimode effects. The VCSEL, on the other hand, appears to be an ideal structure for LBF measurements [Jin et al. (1992)] because it can be designed to have only one cavity mode within the gain and high reflectivity band. The waveguide loss, which is unavoidable in long cavity lasers, can now be avoided or minimized. Moreover, unlike edge emitting lasers whose lasing usually occurs at the peak of the gain curve, a VCSEL can lase only at the single cavity resonance as long as the pump is sufficient to make the gain equal to the loss at that wavelength. Thus the LBF of a microcavity laser can in principle be measured over the entire gain bandwidth.

The fundamental origin of the linewidth broadening factor, α , is the coupling of the real and imaginary part of the dielectric susceptibility of the medium and is given by [Haug et al. (1967)]

$$\alpha(\omega, N) = -\frac{d\chi' / dN}{d\chi'' / dN} \quad (2.1)$$

where N is the carrier density, and ω is the optical frequency. The real and imaginary parts of the total dielectric susceptibility $\chi(\omega, N)$ are given by χ' and χ'' , respectively. From this definition it is seen that α is a material parameter and is both frequency and carrier density dependent. The linewidth of a laser is given by the well known formula [Lax (1967), Haug et al. (1967), Henry (1982)]

$$\Delta\nu = \Delta\nu_{S-T} n_{sp} (1 + \alpha^2) \quad (2.2)$$

where $\Delta\nu_{S-T}$ is the Schawlow-Townes linewidth [Schawlow and Townes (1958)], n_{sp} is the spontaneous emission factor, and one sees the emergence of the α -

parameter. Specifically for semiconductor gain media, it has been shown that the laser linewidth formula given above takes the form [Henry (1982)]

$$\Delta\nu = \frac{v_g^2 h\nu g \alpha_m}{8\pi P_0} n_{sp} (1 + \alpha^2) \quad (2.3)$$

where v_g is the group velocity in the medium, $h\nu$ is the photon energy, P_0 is the single facet output power, g and α_m are the gain and mirror-loss coefficient, respectively. As seen from equation (2.3), $d(\Delta\nu)/d(1/P_0)$ is directly proportional to $(1+\alpha^2)$, allowing a measurement of α by measuring $\Delta\nu$ as a function of P_0 . The other parameters in the equation can be estimated well enough to permit a useful measurement of α .

Another context in which the LBF arises is in the asymmetry in the range of frequency detunings over which injection locking occurs (i.e. larger locking range for positive than negative detuning) [Lang (1982)]. This asymmetry in locking range is again due to the coupling of the real and imaginary parts of the dielectric susceptibility for semiconductor media. It has been shown that the injection locking range can be expressed by [Petitbon et al. (1988)]

$$-\rho < \Delta\omega < \rho(1 + \alpha^2)^{1/2} \quad (2.4)$$

where $\Delta\omega$ is the angular frequency difference between free running VCSEL and injection signal, and α is the LBF. A normalized power term is given by $\rho = (c/2nL) \cdot (P_{inj}/P_{vcSEL})^{1/2}$ where L is the cavity length, n is refractive index of the medium, P_{inj} and P_{vcSEL} are the injection and VCSEL powers, respectively. By comparing the asymmetry in locking range for positive and negative frequency detuning, it is possible to estimate α .

Experimental Method

The GaAs/AlGaAs microcavity laser used in the experiments is the same one described in chapter one. As mentioned there, local growth nonuniformity led to only very few lasing spots. These isolated lasing spots in some cases had quite different operating characteristics across the wafer. The experiments discussed in this section were carried out at the same lasing spot as those described in chapter one thereby allowing better comparison of two techniques of α -parameter measurement. The VCSEL was optically pumped with a threshold of ~ 6.5 mW pump power and lasing wavelength of ~ 885 nm. As mentioned, two methods were used to determine α , linewidth measurements, and injection locking range. The injection locking range experiment was done exactly as described in chapter one. The linewidth measurements were done using an experimental setup very similar to that of chapter one although simpler. The injection signal was not needed and the spectrometer was used only for wavelength calibration. The actual linewidth data as a function of pump power were taken with a Burleigh scanning Fabry-Perot interferometer with 6 GHz free spectral range (finesse ~ 47). A Hamamatsu R1333 photomultiplier tube mounted in a cooled housing ($T \sim -27$ °C, bias = -1.5 kV) was used to detect the light transmitted by the Fabry Perot interferometer. Two Faraday optical isolators were used to prevent feedback to the pump laser (reflection from the sample) and to the microcavity laser (reflection from the Fabry-Perot interferometer).

Analysis

We first analyze the linewidth data. Figure 2.1a shows the nearly linear relationship between the pump power and the VCSEL output power in the range where the linewidth is measured. Figure 2.1b shows that the measured

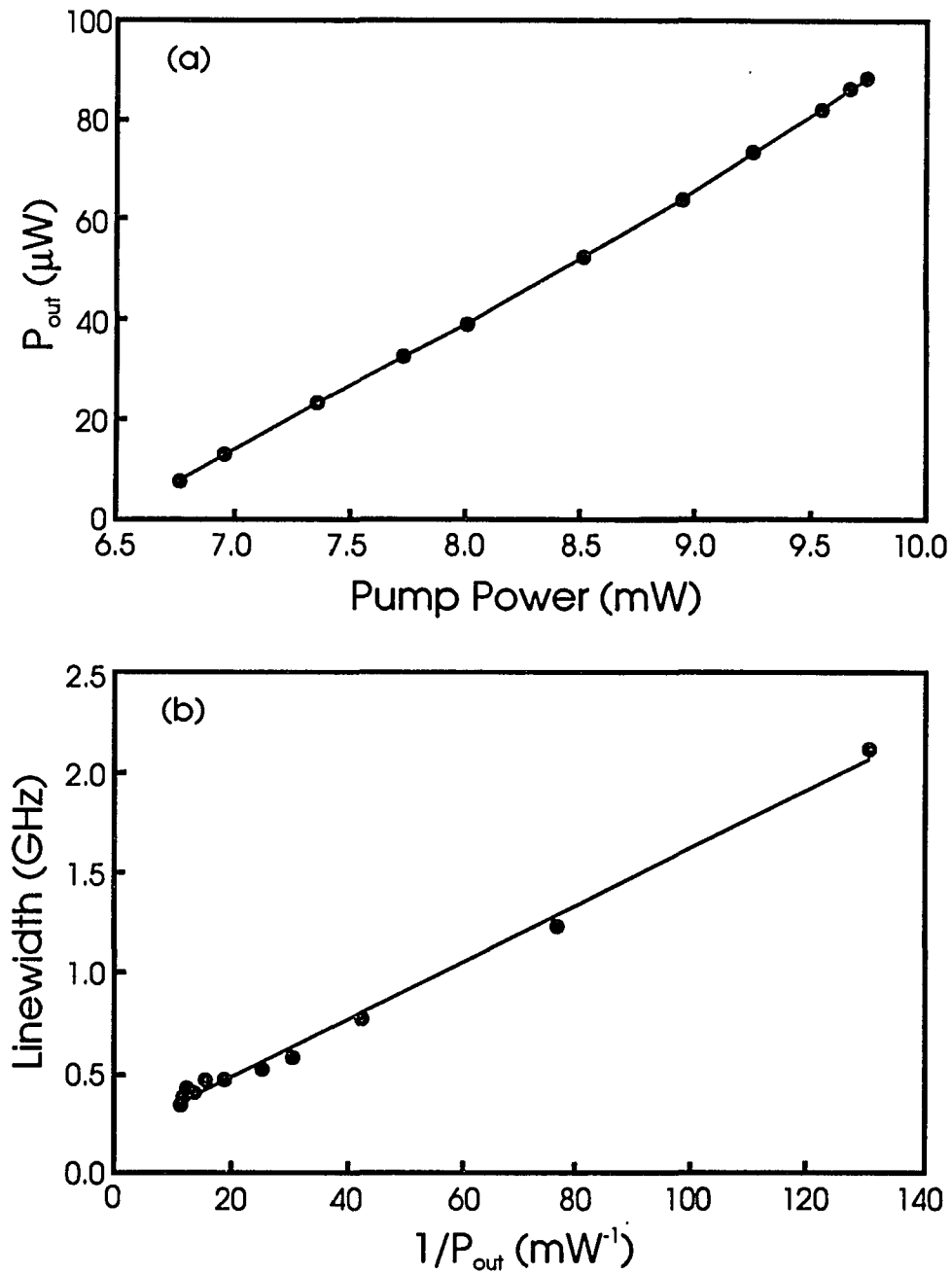


Fig. 2.1 (a) VCSEL output power versus pump power, showing a nearly linear dependence in the power range where linewidth is measured. (b) Linewidth as a function of reciprocal VCSEL output power. The straight line is a least squares fit to the data with slope $14.26 \text{ MHz}\cdot\text{mW}$.

linewidth is proportional to the inverse of the output power of the VCSEL with a slope of 14.26 MHz•mW. To translate this slope to the LBF, we must determine the values of v_g , $h\nu$, g , α_m , and n_{sp} under the experimental conditions. The group velocity, $v_g=c/(n+\omega dn/d\omega)$ [Yariv et al. (1984)], is calculated to be $c/4.85$ at 885 nm [Adachi (1985)]. The photon energy at the SEL lasing frequency is 1.4011 eV. The mirror reflectivity R is determined to be 0.998 by measuring the Fabry Perot width of the cavity, giving $\alpha_m = -(1/L)\ln R = 27 \text{ cm}^{-1}$. The loss α_d due to diffraction is estimated to be about 68 cm^{-1} by calculating the Rayleigh length from the Gaussian beam equations, thus $g = \alpha_d + \alpha_m = 95 \text{ cm}^{-1}$. The carrier density required to produce this gain is about $1.15 \times 10^{18} \text{ cm}^{-3}$ (see Fig. 2.2a) according to plasma theory [Haug et al. (1990), Banyai et al. (1986), Lee et al. (1986a)], which is close to our estimate from experimental conditions. The detuning between laser frequency and the chemical potential is measured [Henry et al. (1980)] to be -9.5 meV, which leads to a spontaneous emission factor (n_{sp}) of 3.26 at room temperature. The resulting slope from equation (2.3) is

$$\frac{d(\Delta\nu)}{d(1/P_0)} = 2.86 \cdot (1 + \alpha^2) \text{ MHz} \cdot \text{mW}. \quad (2.5)$$

Equating this expression to the measured slope of 14.26 MHz•mW, we determine an experimental value of $\alpha = 2.0 \pm 0.5$.

Analysis of the injection locking range data is shown in Fig. 1.4. The reciprocal injection power needed for locking to occur is plotted as a function of frequency detuning of the VCSEL and injection laser. As seen in equation (2.4), the locking range is larger for positive than for negative detuning, which is apparent in the experimental data. From these data, we estimate α to be between

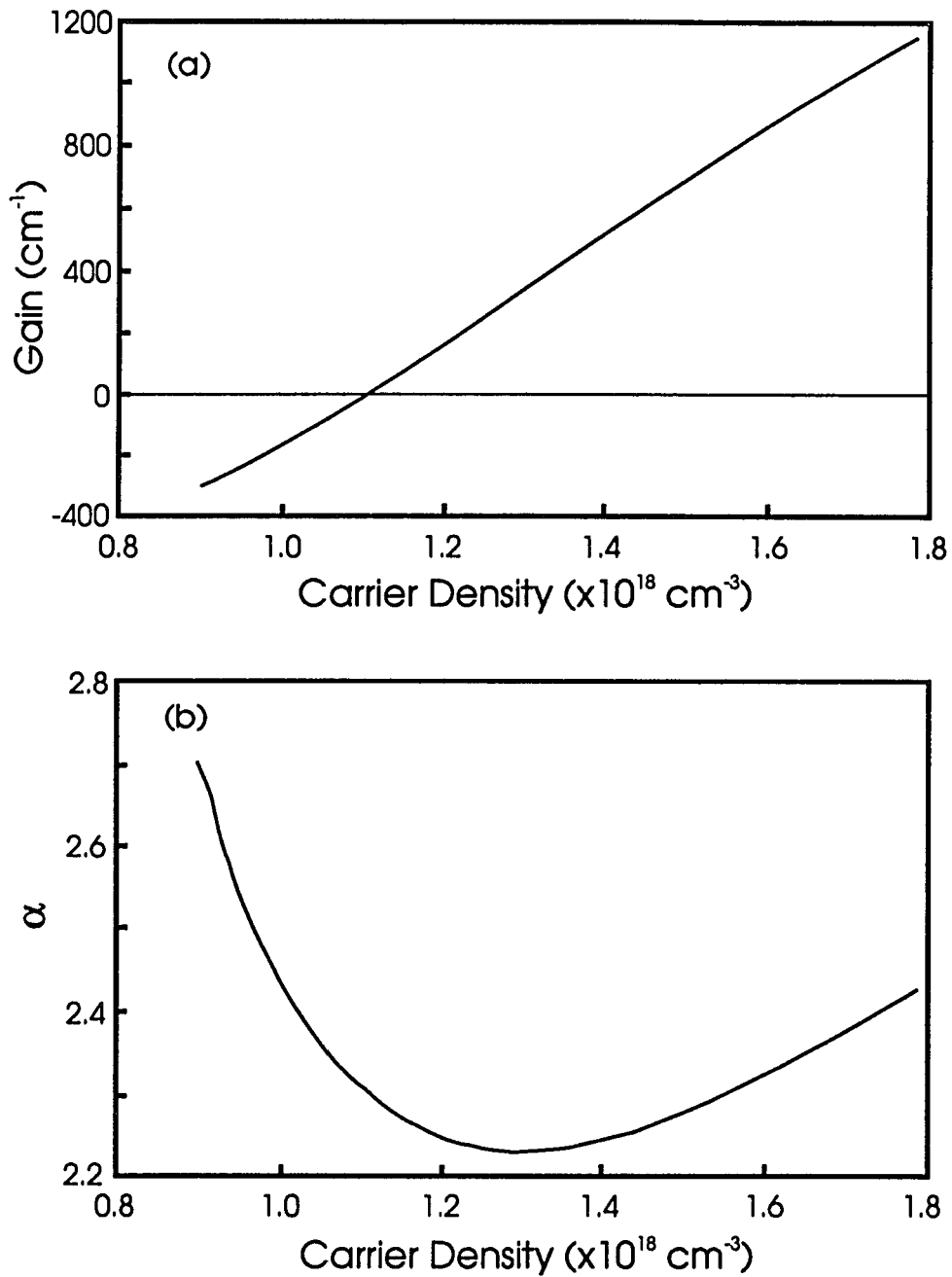


Fig. 2.2 (a) Gain of GaAs at 1.4011 eV for carrier densities relevant for laser operation. (b) Linewidth broadening factor at 1.4011 eV as a function of carrier density. The curves in (a) and (b) are computed using plasma theory.

1.4 and 2.6 which agrees with the value deduced from linewidth measurements. Also shown in this figure is the functional form of the locking range equation (2.4) (solid line) with an assumed value of $\alpha=2.0$.

The LBF computed from the many-body theory is plotted in Fig 2.2b for comparison. The plot shows that the LBF is relatively insensitive to small uncertainties in the carrier density. The experimental value of $\alpha=2.0\pm 0.5$ is in excellent agreement with the theoretical value $\alpha=2.27$ under our experimental conditions. This experiment can also be regarded as a test of the many-body theory of GaAs in the gain region. It is interesting to note that our experimental parameters happen to be such that they cannot be explained by free carrier theory. For example, free carrier theory would not be able to explain a VCSEL lasing frequency of 1.4011 eV, because this value clearly lies on the lower side of the GaAs band gap (1.424 eV) and is due to electronic band gap reduction. The possibility of heating is excluded by varying the amount of average pump power on the VCSEL while keeping the same peak power, and noting that the shift of the lasing frequency is small. On the other hand, many body theory, which includes the effects of plasma screening, bandgap renormalization, as well as bandfilling, does predict a peak-gain frequency shifted by as much as -6 exciton Rydbergs (i.e. -25 meV) from the zero density bandgap, which is in good agreement with the observed lasing frequency. The impressive simultaneous agreement of measured and computed gain frequency, gain magnitude, as well as linewidth broadening clearly illustrates that many-body modifications to the gain spectra are particularly significant in understanding the behavior of microcavity semiconductor lasers.

Summary

Even though α is a material parameter, a direct measurement of α using a mirror-less sample is quite difficult [Pon (1991)]. Using a microcavity laser this becomes relatively easy, and has some intrinsic advantages over conventional techniques. Uncertainties due to waveguiding loss and confinement factor, etc., are greatly reduced or eliminated. With microcavity lasers, the LBF can even be controlled by designing the cavity resonance to be at particular positions in the gain curve. Our experiment is performed on a bulk GaAs VCSEL, but similar measurements with microcavity lasers can be extended to quantum well lasers and other material systems.

Below Threshold Behavior

Introduction

A number of parameters for the design and characterization of microcavity lasers can be measured, however some can at best be estimated by educated guess. Specifically, experimentally finding the carrier densities required for transparency of the active medium and lasing threshold are two important numbers that are difficult to measure. One method to determine transparency at the cavity resonance would be to tune a single frequency probe to the power-dependent peak of the VCSEL Fabry-Perot and measure transmitted intensity as a function of pump power (difficulty in estimating all losses would still lead to some error). With our VCSEL samples the fact that the substrate was not transparent (i.e. bulk GaAs) and that the samples did not lase without proper heat-sinking precluded this option. One motivation to find the transparency carrier density is recent measurements of carrier lifetime in heterostructures and microcavity structures [Yablonovitch et al. (1988), Jin

(1991)]. Knowledge of transparency carrier density is important so that measurements are not carried out in the gain regime where stimulated emission may dominate. This information should also provide clues about sample quality and may prove useful in designing future microcavity lasers for low threshold.

Our technique is experimentally quite simple and relies on the well studied plasma theory to describe band edge nonlinearities of bulk GaAs [Banyai et al. (1986), Lee et al. (1986a), Haug et al. (1990)]. It is well known that generation of carriers (via electrical or optical pump source) causes nonlinear absorption and index changes at the semiconductor absorption band edge. This has been widely studied and developed into many nonlinear etalon devices that work by a change in probe transmission (or reflection) as the Fabry-Perot peak shifts due to nonlinear index change caused by pump beam generated carriers [Gibbs (1985)].

Experimental Method and Analysis

The sample used for these experiments was the same 3λ VCSEL sample described in chapter 1. The experimental setup was also identical to that shown in Fig. 1.1, although much simpler. The optical pump power was provided by the Spectra-Diode Labs 100 mW diode laser. The injection signal was not required and the only spectral analysis equipment used was the 1.26m spectrometer (resolution $<0.1\text{\AA}$) with photon counting PMT (Hamamatsu R943) and associated electronics. This allowed extremely low luminescence light levels to be measured. The photoluminescence of the bulk GaAs active region (generated by optical pump), spectrally filtered by the laser cavity structure, exhibits a narrow Fabry-Perot peak. The Fabry-Perot center wavelength and spectral width obtained from the luminescence spectra were the only

experimental data acquired. From this we deduce other information as described below.

Analysis of the data makes use of the simple Fabry-Perot resonance condition formula

$$2n(\lambda)L = m\lambda_0 \quad (2.6)$$

where L is the cavity length and in this case we know that $m=6$. The refractive index consists of two parts, $n(\lambda)=n_b(\lambda)+\Delta n_{nl}(\lambda)$, where $n_b(\lambda)$ is the background linear index (including dispersion) and $\Delta n_{nl}(\lambda)$ is the nonlinear index change caused by optically generated carriers. At each pump power level we experimentally measure the Fabry-Perot center wavelength, λ_0 , which satisfies equation (2.6). We wish to find the value for $\Delta n_{nl}(\lambda)$ which can be calculated by $\Delta n_{nl}(\lambda)=(3\lambda_0/L)-n_b(\lambda)$ (see Lee et al. (1986b) for a direct measurement of Δn_{nl}). We still have as unknowns the cavity length L and background index dispersion $n_b(\lambda)$. The background index is calculated from the semi-empirical model of Adachi (1985). This model is widely used and yields good agreement with experimental values of bulk GaAs refractive index. Note that at each pump power the center wavelength λ_0 shifts and the background index at this wavelength must be calculated to account for material dispersion. To determine the cavity length, we measure the Fabry-Perot luminescence center wavelength at low pump power levels (facilitated by the sensitive photon counting apparatus). The data points are fit to a polynomial function from which the zero pump power center wavelength is extrapolated. With zero pump, the nonlinear index term is zero leaving all other quantities in (2.6) known so that cavity length can be determined. Now all parameters are known so that Δn_{nl} can be calculated.

In order to actually find the absorption at each pump power level we make use of plasma theory and the Kramers-Kronig relations. Plasma theory allows us to calculate the band edge absorption change caused by carrier generation and the Kramers-Kronig relations allow computation of the associated nonlinear index change. Since we have the experimental nonlinear index change from above, we compare this to the theoretical nonlinear index change and find the absorption and carrier density to which this corresponds.

Results and Discussion

We now present the experimental measurements and their interpretation. Figure 2.3a shows the measured shift of the Fabry-Perot center wavelength as a function of pump power below threshold. The final three points are taken above VCSEL lasing threshold when the wavelength shift is clamped (due to gain clamping). The inset of Fig. 2.3a shows a typical measured luminescence spectrum. In particular, the spectrum shown is when the active medium is transparent (transparency is determined below). Shown in Fig. 2.3b is the Fabry Perot FWHM (full width at half maximum) linewidth as a function of pump power. The unusual feature here is the initial increase in linewidth as the pump power is increased, which is quite unexpected. Two points about the data in Fig. 2.3 need to be made. First, the linewidth when measured very close to threshold approaches the spectrometer instrument limit and is thus a convolution of the actual width and the instrument response function. Secondly, gallium arsenide exhibits a positive nonlinear index change of thermal origin (due to lattice heating and not due to carrier generation). We obtained all data using CW pump light and thus a small positive thermal nonlinear index shift accompanies the larger negative carrier density nonlinear index. This contributes some error to

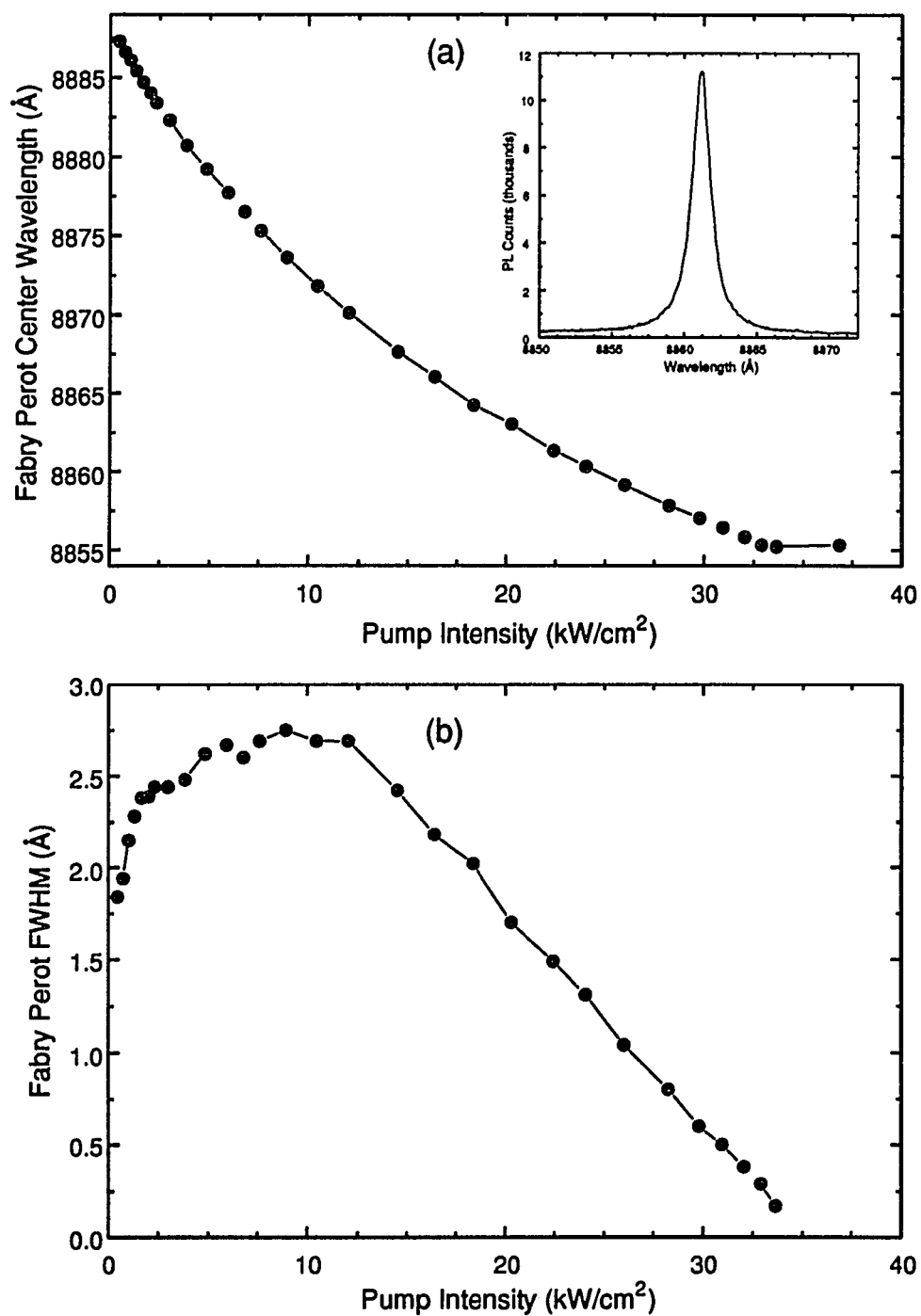


Fig. 2.3 (a) Measured shift of Fabry Perot center wavelength as a function of pump intensity. The inset shows a typical luminescence spectrum. (b) Measured full width at half maximum of Fabry Perot filtered luminescence as a function of pump intensity.

the analyzed data. By taking data during pulsed excitation on a time scale long compared to the carrier lifetime (nsec) and short compared to the thermal time constant (microseconds), this source of error can be eliminated.

By using the procedure described above, we calculate the active region cavity length to be $L=7369 \text{ \AA}$ (from the data of Fig. 2.3a). By using the refractive index model of Adachi we now compute the nonlinear index Δn_{nl} which is shown in Fig. 2.4a. Next, making use of plasma theory and Kramers-Kronig relations we find the carrier density required to achieve the nonlinear index change for the particular wavelength of each point in Fig. 2.4a (a personal computer based plasma theory program developed by the group of S. W. Koch was used for these calculations). Parameters used in plasma theory calculations include a carrier density dependent broadening term given by $\Gamma=\Gamma_0+\Gamma_1N$, where we have used $\Gamma_0=1.25E_R$ and $\Gamma_1=1\times 10^{-18}E_R \text{ cm}^{-3}$ ($E_R=4.2 \text{ meV}$). The Γ_0 term is determined by fitting the linear absorption spectrum, however the value of the Γ_1 term is not well known. This adds some uncertainty to the exact numerical values determined below but does not repudiate the general method. Curves until now shown as a function of pump power can now be translated to functions of carrier density. Nonlinear index as a function of carrier density is shown by the dark line in Fig. 2.4b. Also shown in the figure are plasma theory calculated curves (dashed lines) of nonlinear index for fixed wavelengths. Note that the actual nonlinear index curve for the VCSEL lies between these fixed wavelength curves due to the index dispersion of bulk GaAs.

Now that the nonlinear index is known, we can go back to find the absorption change (and net absorption) that caused the nonlinear index change for each particular wavelength. The net absorption (or gain) as a function of

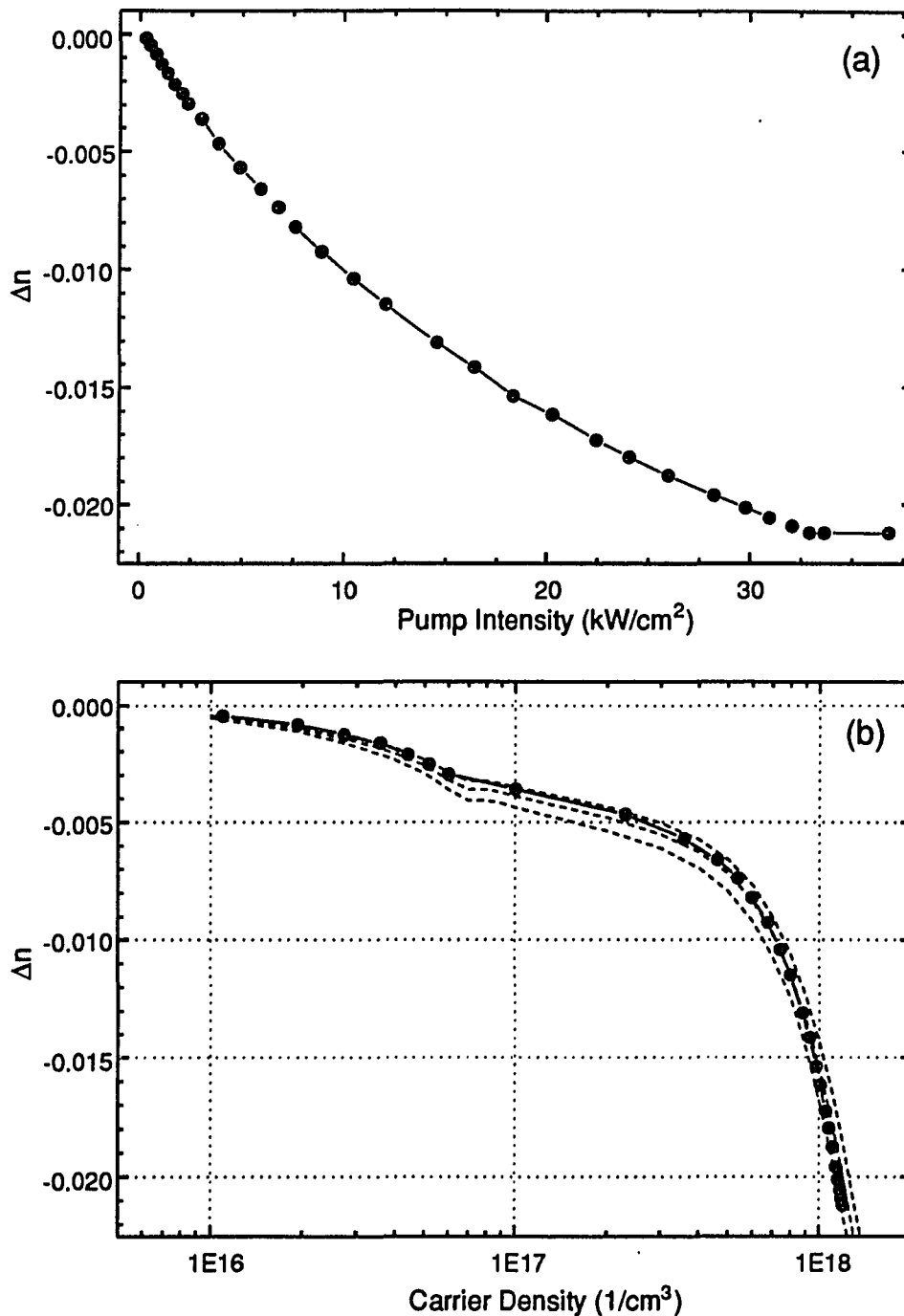


Fig. 2.4 (a) Calculated refractive index change from the shift of Fabry Perot center wavelength data. (b) Refractive index change as a function of carrier density calculated using plasma theory (solid line and dots). The dashed lines are theory curves for fixed wavelengths near the VCSEL lasing wavelength ($\lambda=8894 \text{ \AA}$, 8876 \AA , and 8858 \AA top to bottom).

carrier density is shown by the dark line in Fig. 2.5a. Again, the dashed lines represent absorption calculated by plasma theory for fixed wavelengths (same wavelengths as in Fig. 2.4b). Once more the actual VCSEL absorption/gain curve lies between the fixed wavelength curves. The unusual feature seen here is increasing absorption as carrier density is increased for wavelengths below the zero density bandgap. Physically this is caused by line broadening and provides an explanation for the increase in Fabry-Perot linewidth shown in Fig. 2.3b. The effective reflectivity $R_{\text{eff}}=Re^{-\alpha L}$ of the cavity mirrors is decreased by absorption in the active region which causes broadening of the linewidth. The shape of the curves for active region absorption and Fabry Perot linewidth overlap fairly well for carrier densities above approximately $5 \times 10^{17} \text{ cm}^{-3}$ as shown in Fig. 2.5b. Since only the shift of the Fabry-Perot center wavelength is used to determine carrier density and absorption, the overlap of the linewidth curve in Fig. 2.5b induces some confidence in the data analysis method.

From the above curves we can determine several other important pieces of information. The carrier density at laser threshold is approximately $N_{\text{th}} \approx 1.19 \times 10^{18} \text{ cm}^{-3}$. We also find that transparency ($\alpha=0$) occurs at a carrier density of $N_0 \approx 1.05 \times 10^{18} \text{ cm}^{-3}$. The Fabry Perot linewidth (FWHM) at transparency is 1.5 \AA . Since the cavity is empty (no absorption or gain) we can use the ordinary Fabry Perot linewidth formula to find the actual reflectivity of the cavity mirrors. The high reflectivities of VCSEL mirrors (>99%) are difficult to measure in practice, but such knowledge is an important indicator of the quality of MBE growth. The calculated reflectivity from the linewidth measurement for this exceptional spot is $R=0.997$ (assuming a symmetric cavity).

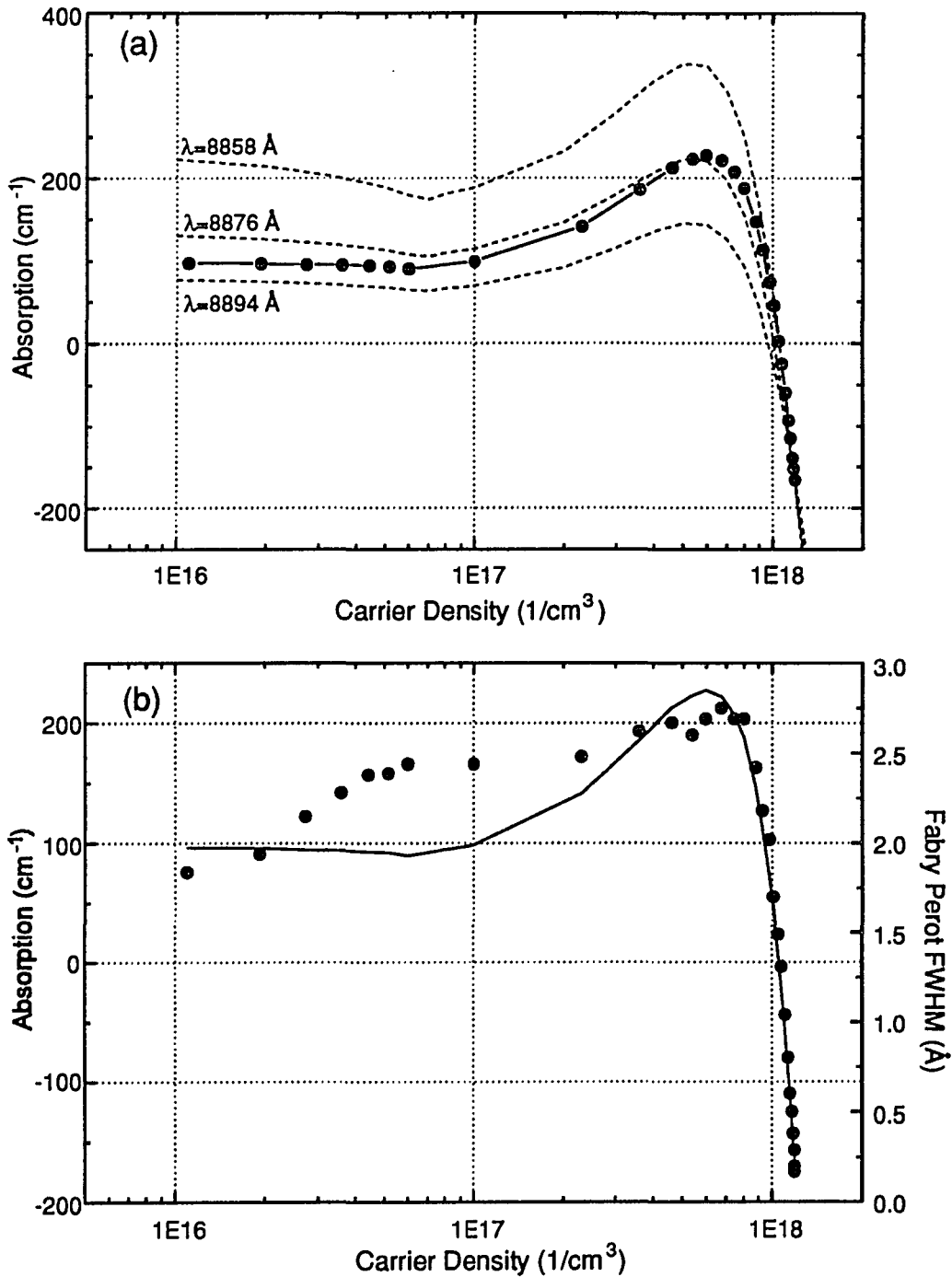


Fig. 2.5 (a) Absorption as a function of carrier density as deduced from plasma theory corresponding to the nonlinear index of above (circles and solid lines). The dashed lines are theory curves for fixed wavelengths. (b) Overlap of the curves for absorption as a function of carrier density (solid line) and Fabry-Perot width as a function of carrier density (circles).

Carrier lifetime is a subject of intense study especially recently in regard to modified spontaneous emission decay rates in microcavities. Studies in atomic systems have shown conclusive proof of cavity modified decay rates [Hulet et al. (1985)]. However, in room temperature semiconductor systems the situation is complicated by the fact that the bimolecular recombination process implies a carrier density dependent lifetime. As such, precise knowledge of carrier density is required with any measurement of lifetime. Initial motivation for this work was to find carrier density information to complement time-resolved luminescence lifetime measurements. Since plasma theory calculations depend only on carrier density and have no connection with lifetime, it was realized that by extending the above analysis it was possible to deduce carrier lifetime as a function of carrier density.

The standard rate equation describing carrier generation and decay is [Agrawal et al. (1986)]

$$\frac{dN}{dt} = \frac{\alpha_p I_p}{h\nu_p} - \frac{N}{\tau_{eff}} \quad (2.7)$$

where the first right hand side term describes optical generation of carriers and the second term decay of carriers. An effective lifetime τ_{eff} is used in this equation to describe all decay processes. The decay term is usually expanded in a power series, $N/\tau_{eff} = A_{nr}N + B(N)N^2 + CN^3$, where the first term is attributed to nonradiative decay, the second term to bimolecular recombination (spontaneous emission), and the final term to Auger recombination. Notice that the bimolecular recombination coefficient, $B(N)$, is carrier density dependent. The nonradiative coefficient has been estimated $\tau_{nr} = 1/A_{nr} > 30$ nsec [Chavez-Pirson (1989)], which allows us to drop this term for the carrier density range we

are interested in. The small Auger recombination coefficient, $C < 2 \times 10^{-30} \text{ cm}^6/\text{sec}$ [Olshansky et al. (1984)], allows us to drop this term leaving only the bimolecular term. Ordinarily, a carrier lifetime is defined at this point by $\tau_c = 1/B(N)N$, which allows us to rewrite the above expansion as $N/\tau_{\text{eff}} = N/\tau_c$. We can now solve (2.7) in steady state to find the carrier lifetime $\tau_c = Nh\nu_p/\alpha_p I_p$.

To determine the lifetime we use $\tau_c = (N - N_{\text{lin}})h\nu_p/(\alpha_p I_p)$ where we have subtracted the small correction term $N_{\text{lin}} (= 1.0 \times 10^{15} \text{ cm}^{-3})$ which is the carrier density assumed in plasma theory to calculate linear absorption spectra. We use values of pump wavelength of $\lambda_p = 8270 \text{ \AA}$, pump absorption coefficient $\alpha_p = 12300 \text{ cm}^{-1}$ (determined from plasma theory linear absorption), and a $20 \mu\text{m}^2$ spot area in determining pump intensity (Lifetime calculation requires knowledge of pump power and spot size, quantities not needed until now. Pump power was measured using a precision digital power meter; spot size was estimated using the objective focal length and assuming the diffraction limit.). Carrier density N has already been determined above for each pump intensity. The resulting carrier density dependent carrier lifetime is shown in Fig. 2.6 (for densities greater than $\sim 5 \times 10^{17} \text{ cm}^{-3}$, corresponding to the range where Fabry-Perot linewidth and absorption curves overlap in shape - see Fig. 2.5b).

A few words of caution are required here in interpreting the numbers shown in Fig. 2.6. One is usually interested in the spontaneous emission lifetime (bimolecular recombination), commonly measured by luminescence decay after pulsed excitation. The technique we have used to deduce carrier lifetime does not distinguish the physical processes involved in carrier relaxation. In addition to the radiative processes of spontaneous emission below transparency and stimulated emission in the gain regime, another physically important relaxation

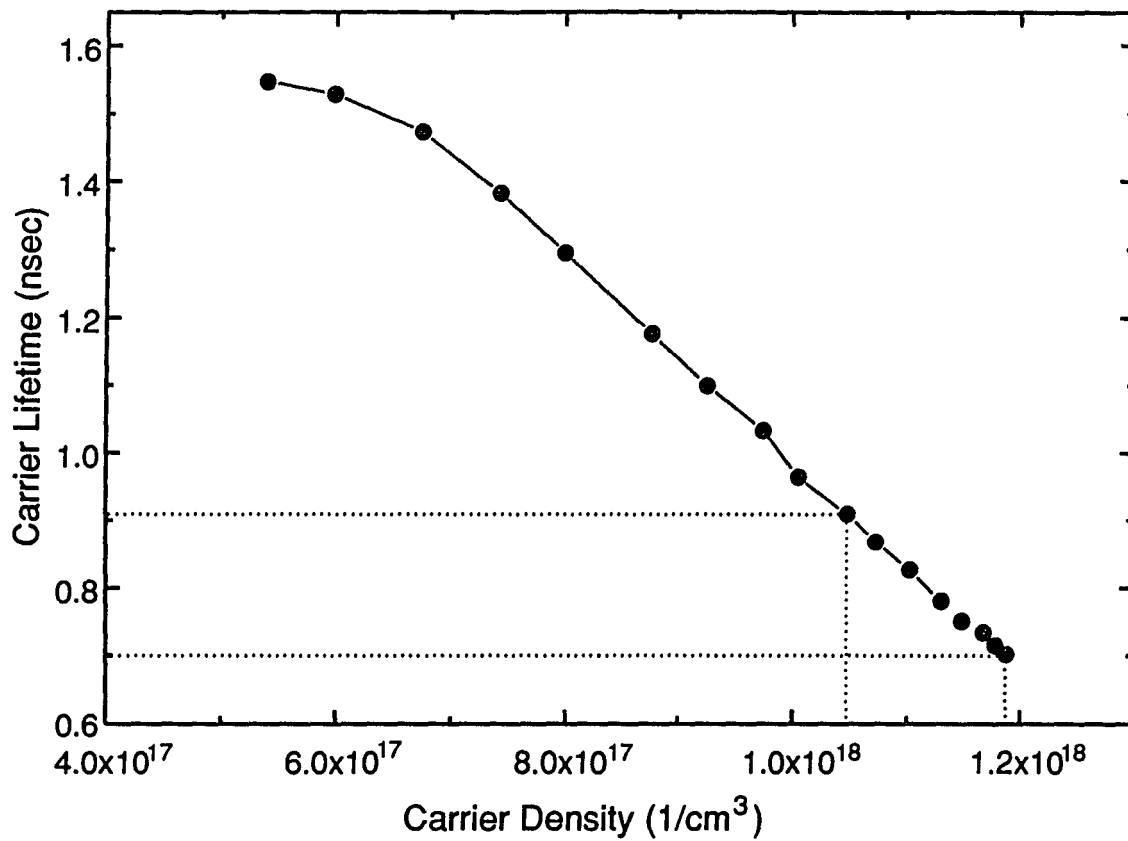


Fig. 2.6 Carrier lifetime as a function of carrier density. The dotted lines point out transparency ($\tau=0.9$ nsec) and threshold ($\tau=0.7$ nsec).

mechanism is carrier diffusion out of the pump spot. Due to the high density of carriers (near the transparency region) the possibility of cooperative emission effects leading to enhanced decay rates has also recently come under discussion. With this said, the carrier lifetime numbers in Fig. 2.6 must necessarily be considered an effective lifetime due to all decay processes and not only bimolecular recombination. However, from this very simple measurement, one is able to simultaneously determine both carrier density and carrier lifetime. Specifically, at transparency the lifetime is $\tau \sim 0.9$ nsec and at lasing threshold $\tau \sim 0.7$ nsec.

Summary

A very simple technique of measuring shift of Fabry-Perot peak to determine VCSEL parameters seems to be fairly good at extracting useful information with reasonably small error. The overlap of absorption and Fabry-Perot linewidth curves engenders some degree of confidence in this method. Numerical values for carrier density at threshold and mirror reflectivity are within reasonable expectations. The data on carrier lifetime as a function of density are interesting and need to be complemented by time-resolved luminescence lifetime measurements to clarify the mechanisms of bimolecular recombination coefficient dependence on carrier density.

CHAPTER THREE

PHOTON NUMBER CORRELATIONS NEAR THRESHOLD

Introduction

"Nature abhors a vacuum." -F. Rabelais (16th century). The importance of the vacuum has been recognized for centuries in diverse contexts. Only in this century has the essence of the vacuum been understood, as quantization came to light. In quantum optics, atom-vacuum field coupling is of fundamental significance. Indeed, spontaneous emission by an atom may be viewed as being stimulated by the zero-point energy fluctuations of the vacuum.

Cavity quantum electrodynamics (QED), the study of radiative properties of atoms in tailored electromagnetic environments, has blossomed as a field of study in recent years with stunning experimental and theoretical success [Meystre (1992), Haroche (1992)]. Effects of cavity QED become manifest when atoms (or other active media) are immersed in high-Q resonant cavities of length on the order of emitted radiation wavelength. Initial studies with Rydberg atoms in the microwave regime and a trapped single electron in microwave cavity [Kleppner (1981), Hulet et al. (1985), Gabrielse et al. (1985)] evolved to the beautiful work on the micromaser [Meschede et al. (1985)]. These successes prompted others to seek similar effects in the optical wavelength regime using atomic systems [Heinzen et al. (1987a)] and inspired thoughts on analogous effects in solid state [Yablonovitch (1987)]. Modified spontaneous emission rates (both enhanced and inhibited), vacuum Rabi splitting (reversible spontaneous

emission) [Raizen et al. (1989), Weisbuch et al. (1992)], and atomic level shifts [Heinzen et al. (1987b)] are a few of the varied phenomena observed.

We wish to concentrate on the cavity modified spontaneous emission rate mentioned above (first pointed out by Purcell (1946)). The physical origin of this effect is that the cavity can significantly alter the density of states to which the atom may couple relative to the continuum of free-space modes assumed in the Weisskopf-Wigner spontaneous emission calculation [Meystre and Sargent (1991)]. The experimental success in modifying decay rates stimulated further thought regarding laser operation. The concept of a laser without threshold arose as it was argued that by inhibiting active medium coupling to nonlasing modes (by proper cavity design), all emitted light (whether stimulated or spontaneous) would only be into the remaining laser mode [De Martini et al. (1988)]. A similar type of argument was put forth by Yablonovitch (1987) in proposing the full 3D photonic bandgap concept (optical analogue of an electronic bandgap) in which the density of optical modes is reduced to zero. In such a medium, all emission would be forbidden (realized experimentally in the microwave regime by Yablonovitch et al. (1989)).

The concept of threshold-less lasing has gained favor amongst the semiconductor microcavity laser community and the standard semiclassical rate equations of a semiconductor laser have been used to model the situation [Yokoyama et al. (1989), Bjork et al. (1991)]

$$\frac{dN}{dt} = \frac{\alpha_p I_p}{h\nu_p} - \frac{N}{\tau} - gS \quad (3.1)$$

$$\frac{dS}{dt} = \left(g - \frac{\nu}{Q}\right)S + \beta \frac{N}{\tau}. \quad (3.2)$$

The first equation for carrier density, N , includes terms to account for optical pumping of carriers (first term RHS), spontaneous emission (second term RHS) and stimulated emission (last term RHS). The second equation for photon number, S , includes stimulated emission (first term), cavity loss (second term), and spontaneous emission (final term). The linear density gain model, $g=a(N-N_0)$, is used, where a is in units of cm^3/sec and N_0 is the transparency carrier density. The other terms are: I_p -pump intensity, α_p -absorption at pump wavelength, τ -carrier lifetime, Q -cavity energy storage. Admittedly, this is a very simple model and does not take into account many properties of the real semiconductor medium, but serves to illustrate a few points.

We now address the parameter known as the spontaneous emission factor, β , in the previous equation. By definition the spontaneous emission factor is given by

$$\beta = \frac{\text{spont. emission into lasing mode}}{\text{total spont. emission}} \quad (3.3)$$

This parameter has become of central importance in discussing microcavity lasers as it is used to account for coupling to nonlasing modes. Using a classical electromagnetic formalism, the β -factor for ordinary edge-emitting semiconductor lasers has been approximated by [Suematsu et al. (1977)]

$$\beta \cong \frac{\lambda^4}{4\pi^2 V_a \Delta\lambda n^3} \quad (3.4)$$

where λ is the emission center wavelength, V_a is the active region volume, $\Delta\lambda$ is the spontaneous emission linewidth, and n is the index of refraction. For a typical edge emitting laser, $\beta \sim 10^{-5}$, i.e. one in 10^5 spontaneously emitted photons is coupled into the lasing mode. Calculating the specific density of

optical modes from first principles for each particular cavity geometry is rather difficult and still an area of research [DeMartini et al. (1991), Baba et al. (1991), Baba et al. (1992)]. Therefore β is used as a phenomenological factor in this simple model. As emission into nonlasing modes is inhibited, β increases (to a possible maximum of unity).

Solving the previous set of rate equations in steady state with parameters for a typical GaAs microcavity laser and various values of β , we get the set of curves shown in Fig. 3.1. The output power versus input power curve of Fig. 3.1a shows a typical threshold knee for $\beta=10^{-4}$, but for high β ($=0.9$) essentially looks like a straight line. For most conventional lasers the sharp knee in the output power curve is indicative of threshold and is quite easy to identify. The smooth shape of the high β curve, with no defining features, leads to the claim of threshold-less lasing. Shown in Fig. 3.1b is the carrier density as a function of pump power. For the low β ($=10^{-4}$) case, carrier density is clamped once threshold is reached, as expected. However, in the high β case carrier density does not strictly clamp at any particular pump value but approaches an asymptotic limit. It has also been suggested that one may obtain lasing without population inversion for the high β case [Yamamoto et al. (1992)] (The output power for $\beta=0.9$ follows an almost straight line in Fig. 3.1a even when the carrier density in Fig. 3.1b is below transparency $N_0 \sim 1.05 \times 10^{18} \text{ cm}^{-3}$. This simple model with linear gain approximation is not valid well below transparency and casts doubt on lasing without inversion.). The straight line character of output power is illustrated with this simple model but other conclusions must be regarded with skepticism.

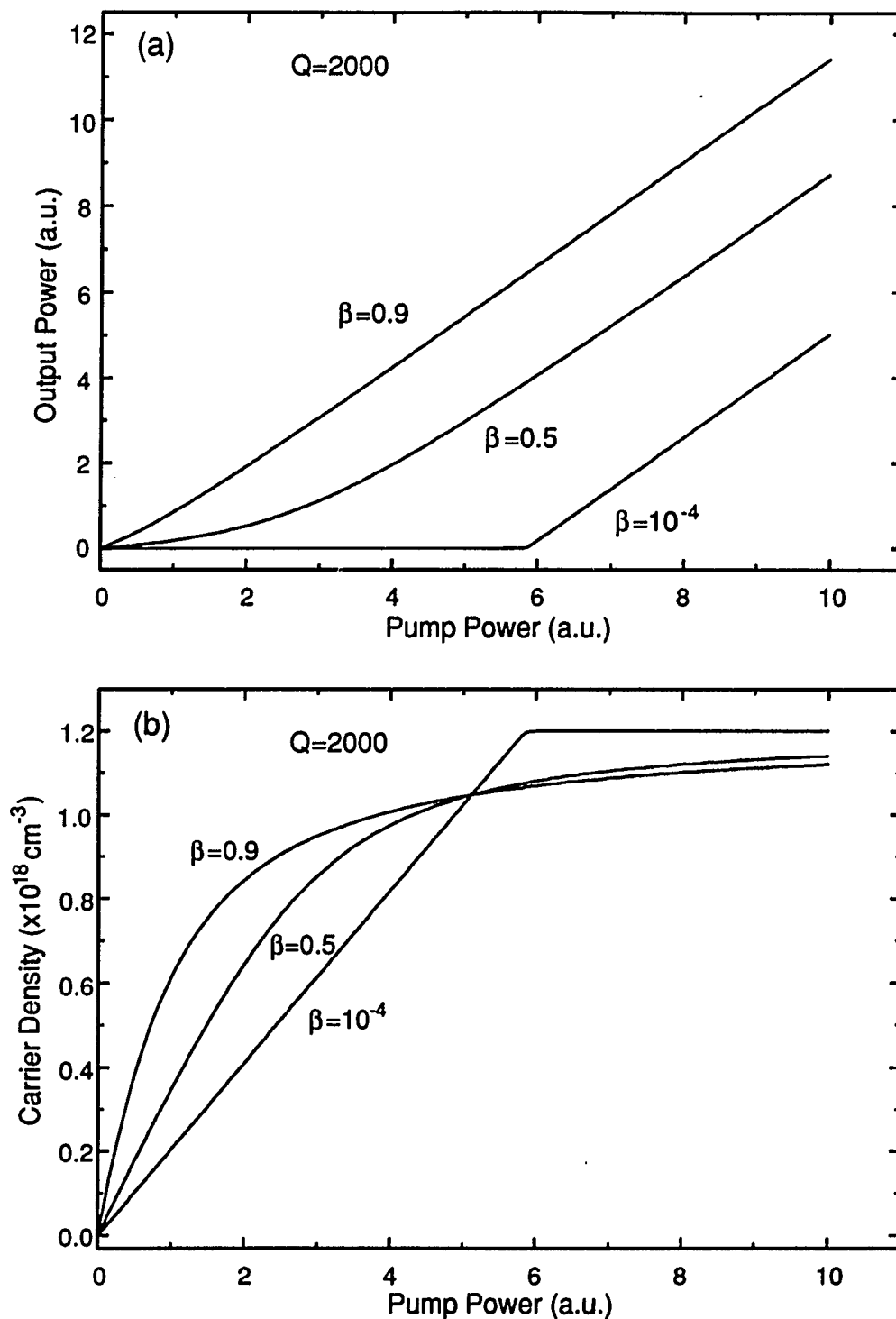


Fig. 3.1 (a) Output power versus pump power for $Q=2000$ and several values of β . (b) Carrier density as a function of pump power (both graphs are obtained using the simple rate equation model).

In order to clarify what is meant by laser threshold, a strict definition is required. Historically, laser threshold has been theoretically described in terms of an analogy between the laser and a nonequilibrium phase transition [de Giorgio et al. (1970), Graham et al. (1970)]. In the thermodynamic limit, it is characterized as a second-order-like phase transition, the derivative of the output intensity as a function of the pump parameter exhibiting a discontinuity at threshold. This feature is quite pronounced for conventional lasers of low β but difficult to distinguish as β increases. Thus, the definition of threshold and the concept of threshold-less remain nebulous for microcavity lasers.

Answers to two important questions must be clarified: 1) What is the fundamental nature of laser light?, and 2) In the context of the answer to the last question, how does one provide a universal definition of threshold applicable to all lasers from the most conventional to the microcavity limit? As explained in any good textbook on laser physics [for example Sargent et al. (1974)], light emitted by a laser well above threshold is characterized as being in a coherent state. The photon statistics of this light follow a Poisson distribution as opposed to the Bose-Einstein distribution followed by light of thermal origin. The laser transition through threshold is marked by the change in its photon statistics, thus pointing to a fundamental definition of threshold.

Theoretical Background

In this section we wish to briefly review some concepts of coherence of light and give an outline of the quantum theory of a two-level laser (with ground lower level). Since the coherence of light is well studied and thoroughly explained in many books (Loudon (1983), Haken (1985), Born and Wolf (1986),

Glauber (1965) to name a few), we only highlight a few relevant points. We begin with the classical first order coherence function given by

$$g^{(1)}(\tau) = \frac{\langle E^*(t)E(t+\tau) \rangle}{\langle E^*(t)E(t) \rangle} \quad (3.5)$$

where the electric field is given by $E(t) = E_0 \exp[-i\omega_0 t + i\phi(t)]$. We will assume all fields to be stationary, thus eliminating dependence on particular times t_1 and t_2 and retaining dependence only on time difference τ (we have also dropped all spatial dependence for simplicity). This coherence function is that which is ordinarily measured in a Young's double slit experiment. Since this is field amplitude interference, phase information of the light source is retained. For example, a collision-broadened Lorentzian lineshape light source (of spectral width $1/\tau_0$) will have first order coherence given by $g^{(1)}(\tau) = \exp[-i\omega_0 \tau - (2\tau/\tau_0)]$ [Loudon (1983)].

The classical second order coherence function is given by

$$g^{(2)}(\tau) = \frac{\langle E^*(t)E^*(t+\tau)E(t+\tau)E(t) \rangle}{\langle E^*(t)E(t) \rangle^2} = \frac{\langle I(t)I(t+\tau) \rangle}{I^2} \quad (3.6)$$

where $I(t)$ is now the field intensity. Notice that in this case the intensity of the incident light is measured and phase information is lost. Two important properties of this classical function are: 1) $g^{(2)}(0) \geq 1$, and 2) $g^{(2)}(\tau) \leq g^{(2)}(0)$. For "chaotic" (thermal) light sources, the second order coherence function can be expressed in terms of the first order correlation function

$$g^{(2)}(\tau) = 1 + |g^{(1)}(\tau)|^2 \quad (3.7)$$

which implies a limiting value of unity for $g^{(2)}(\tau)$ as τ gets large. It can also be shown from (3.7) and (3.5) that $g^{(2)}(0)=2$ (for "chaotic" light). No such relation as (3.7) can be derived for non-"chaotic" light sources (e.g. laser light).

Field quantization is required to completely describe the wave-particle nature of light. Second order coherence properties of light examined with quantized fields may sometimes yield non-intuitive results. We follow the ordinary decomposition procedure into positive, $\hat{E}^+(t)$, and negative, $\hat{E}^-(t)$, frequency component field operators, where $\hat{E}^+(t)$ contains the annihilation operator \hat{a} and $\hat{E}^-(t)$ contains the creation operator \hat{a}^+ [Cohen-Tannoudji et al. (1989)]. The quantized first order coherence function is now

$$g^{(1)}(\tau) = \frac{\langle \hat{E}^-(t)\hat{E}^+(t+\tau) \rangle}{\left[\langle \hat{E}^-(t)\hat{E}^+(t) \rangle \langle \hat{E}^-(t+\tau)\hat{E}^+(t+\tau) \rangle \right]^{1/2}} \quad (3.8)$$

and yields identical answers to the classical version in all respects. The second order coherence function is given by

$$g^{(2)}(\tau) = \frac{\langle \hat{E}^-(t)\hat{E}^-(t+\tau)\hat{E}^+(t+\tau)\hat{E}^+(t) \rangle}{\langle \hat{E}^-(t)\hat{E}^+(t) \rangle \langle \hat{E}^-(t+\tau)\hat{E}^+(t+\tau) \rangle} \quad (3.9)$$

but now the range $1 > g^{(2)}(\tau) \geq 0$ is not strictly forbidden. We will be primarily interested in the second order coherence at zero time delay ($\tau=0$) which allows us to simplify (3.9) to

$$g^{(2)}(0) = \frac{\langle \hat{n}(\hat{n}-1) \rangle}{\langle \hat{n} \rangle^2} = \frac{\overline{n^2} - \bar{n}}{\bar{n}^2} \quad (3.10)$$

where $\hat{n} = \hat{a}^\dagger \hat{a}$ is the number operator and \bar{n} is the mean number of photons. We introduce the Fano-Mandel parameter [Meystre (1992), Mandel (1982)], K , given by

$$K = \frac{\overline{n^2} - \bar{n}^2 - \bar{n}}{\bar{n}} = \bar{n} [g^{(2)}(0) - 1], \quad (3.11)$$

which we wish to measure experimentally as a function of pump power (the first experimental measurements near threshold were made by Armstrong and Smith (1965a, b)).

To measure the second order coherence of light, a single light beam is split into two equal parts and detected by two identical detectors, with the resultant detector outputs electronically correlated (see Fig. 3.2 and further description below). The first experimental measurement of the second order coherence of light was made by Hanbury Brown and Twiss using a technique similar to that described above (now known as the Hanbury Brown - Twiss interferometer), which measures $g^{(2)}(\tau) - 1$ [Hanbury Brown and Twiss (1958), Hanbury Brown (1974) and references therein]. The intensity interference process can be viewed either classically in terms of waves or quantum mechanically in terms of photons, giving identical results for ordinary light sources. Classically, the incident light wave is split into two identical portions by the beamsplitter and the envelope of intensity fluctuations of the incident beam are electronically correlated as a function of time delay. In the quantum mechanical picture, an incident photon is either transmitted or reflected by the beamsplitter and strikes a single detector. Light with a value of $g^{(2)}(0) > 1$ is known as bunched; $g^{(2)}(0) < 1$ is anti-bunched (a pure quantum mechanical effect); and $g^{(2)}(0) = 1$ is coherent light (laser light).

We now give an overview of the quantum theory of a two-level laser. Since we are interested in cavity QED effects in such lasers we first classify our regime of operation with the help of three rates called γ' , κ , and g . The spontaneous emission rate into free space modes in the presence of a cavity is given by γ' , which is related to the cavityless free space spontaneous emission rate γ by a geometrical factor which depends on the solid angle sustained by the resonator (γ' can be related to β as shown below). Resonator losses are given by κ , and g is a measure of the dipole coupling between atoms and the cavity mode. Two main regimes of cavity QED can then be identified: in the weak coupling regime, g is smaller than one of the decay rates κ and γ' , where γ' can be significantly different from γ ; and in the strong coupling regime, g is the dominant rate. In contrast, conventional quantum optics and laser physics is characterized by the inequality $g < \gamma', \kappa$. The strong coupling regime has been explored with the micromaser and reversible spontaneous emission experiments mentioned earlier. The weak coupling regime is characterized by irreversible spontaneous emission, but possibly enhanced or inhibited. This is the regime in which the "threshold-less" laser limit has been proposed when $\gamma' \rightarrow 0$.

The quantum theory of a microlaser operating in the weak coupling cavity QED regime is straightforward in principle. The active medium is coupled to two baths, one which describes spontaneous emission into the free space modes and gives rise to the decay rate γ' , and the other which describes damping of the cavity mode at rate κ [Carmichael et al. (1986)]. In addition, the active medium is coupled to the field mode with the coupling constant g . Since we are in the weak coupling regime, all standard approximations of laser theory can still be carried out, and the only effective changes are in the various decay

rates entering the equations. The photon statistics are derived via a quantum theory based on the density matrix equations of motion [Scully et al. (1967), Sargent et al. (1974)]. Two remarks need to be made at this point: First, the transverse relaxation rate $1/T_2$ of the atomic transition depends in general both on elastic collisions and on spontaneous emission, and hence is changed from its free space value in cavity QED situations. However, if the laser medium is collision dominated, such as in semiconductor lasers, we can neglect the effects of spontaneous emission and use the free space-value of this rate. Second, the rate γ is quite complicated to compute from first principles for a given cavity geometry, and is treated as a phenomenological factor here.

We consider specifically the case of a two-level laser with upper-to-ground-lower-level decay [Meystre and Sargent (1991)]. This configuration describes the three-level pumping scheme appropriate for the ruby laser as well as some aspects of the semiconductor laser, for which the pump occurs directly from the valence band to the conduction band. We assume that the upper laser transition is pumped at rate Λ from the lower state (e.g. through a fast decaying third level) and that both thermal baths are at zero temperature, an excellent approximation in the optical regime. The photon-number probability p_n is then readily found to be

$$\frac{dp_n}{dt} = -(n+1)A_{n+1}p_n + (n+1)B_{n+1}p_{n+1} + nA_n p_{n-1} - nB_n p_n \quad (3.12)$$

where n is the photon number and $A_n = N_a R / 2T_1(1+nR)$, $B_n = N_b R / 2T_1(1+nR)$, $N_a = N' \Lambda T_1$ and $N_b = N' \gamma T_1$ are the normalized zero-field populations of the upper and lower laser levels, with $T_1 = (\Lambda + \gamma)^{-1}$, $R = 4g^2 T_1 T_2$ ($g^2 = \pi^2 \wp^2 E_\omega^2 / 2\hbar^2$, where \wp , E_ω and \hbar are the dipole matrix element, the electric field per photon,

and Planck's constant, respectively), with N' being the total number of atoms contributing to lasing. By substituting the parameters of this theory into the basic definition of β given in (3.3), we find by $\beta=(1+\gamma/2g^2T_2)^{-1}$. In steady state, the master equation yields the photon statistics

$$p_n = p_0 \prod_{k=1}^n \frac{N_a}{N_b + 2T_1(R^{-1} + k)\kappa} \quad (3.13)$$

where p_0 is the probability of no photon, and acts as a normalization constant. We concentrate here on the second moment of the photon statistics, and specifically compute the Fano-Mandel parameter given in (3.11). These results are then compared with measurements carried out with a GaAs microcavity laser operating in a range where our simple two-level laser theory can give reasonable results [Jin et al. (1993)].

Experimental Method

As described above, we wish to experimentally measure the Fano-Mandel parameter K of light emitted by the VCSEL. In theory, this measurement is expressed by one simple equation (3.11). However, in practice the experimental details are nontrivial, and we describe our method here. We construct a version of the Hanbury Brown - Twiss interferometer using a photon counting technique with coincidence counter (see Fig. 3.2).

The VCSEL sample was the same 3λ sample previously discussed in chapter one, but a different spot on the sample was used. The lasing wavelength was $\sim 8835 \text{ \AA}$, with threshold pump power of approximately 6.8 mW. The optical setup to provide optical pump power to the sample was the same as in chapter one. The pump laser diode was operated at fixed current ($i \sim 110 \text{ mA}$) and temperature ($T \sim 14.9 \text{ }^\circ\text{C}$) and was protected from optical feedback by an optical

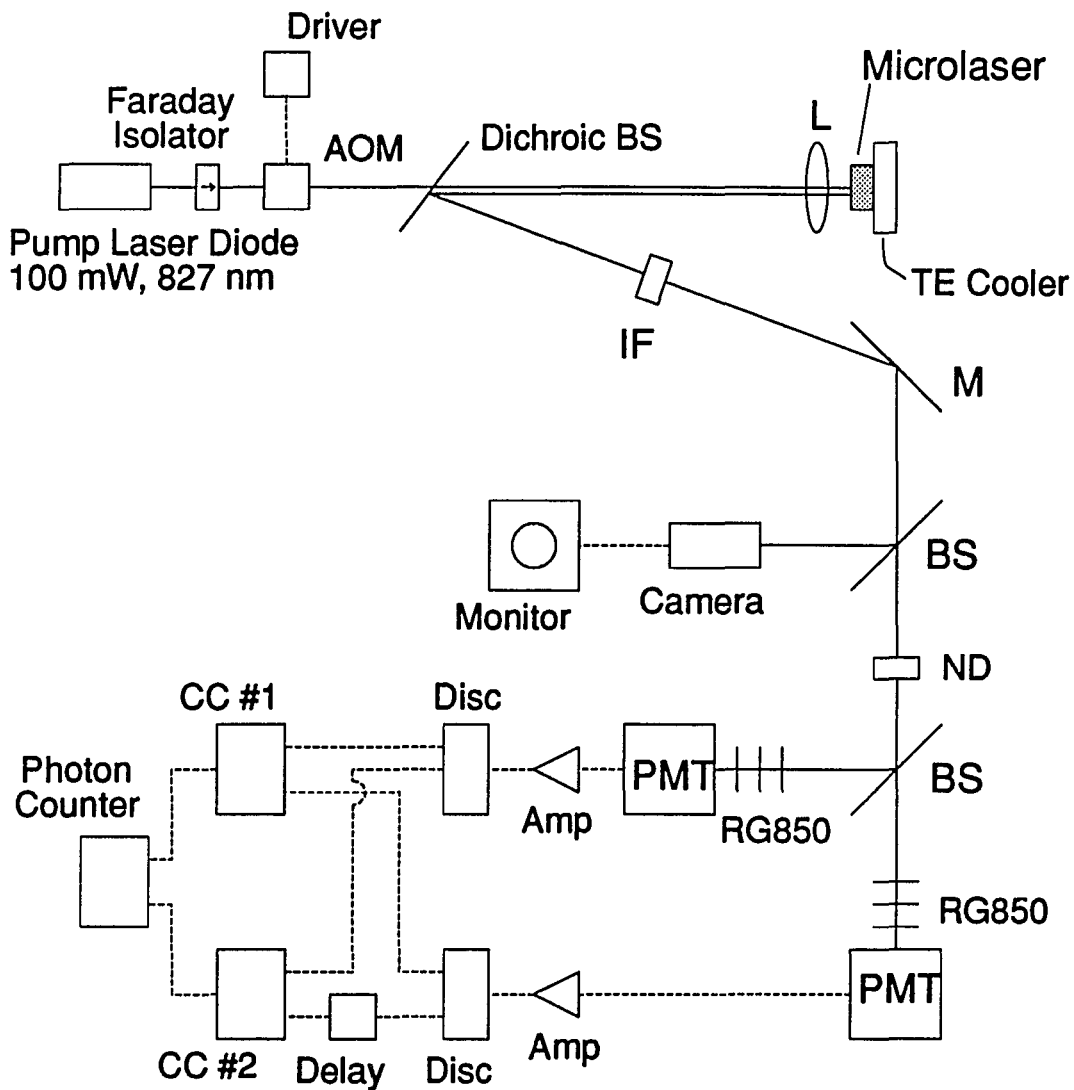


Fig. 3.2 Experimental setup used to measure photon number correlations. AOM- acousto-optic modulator; IF-interference filter; BS-beam splitter; L-lens; TE- thermo-electric; M-mirror; ND-neutral density filter; RG850-long pass edge filter; PMT-photomultiplier tube; Amp-amplifier; Disc-discriminator; CC-coincidence counter.

isolator. An acousto-optic modulator (AOM) in the pump beam path was used to control intensity. To provide high pump power stability, the 50Ω input impedance of the AOM controller was driven by the output of a stabilized constant current laser diode power supply. The pump light passed through a dichroic beamsplitter which reflected and thus spatially separated the VCSEL lasing.

A high contrast interference filter (center wavelength 880nm, bandwidth 10nm) was placed in the VCSEL output beam to remove any residual pump light before reaching the actual detection equipment. The VCSEL light passed through a variable neutral density wheel and was split by a 50/50 beamsplitter. Each of the two beampaths were measured to be of equal length after the beamsplitter and directed to photomultiplier tubes (PMT). Three RG850 edge filters were placed before each PMT to filter any stray light in the room. Each PMT was mounted in a shielded enclosure and water cooled to reduce thermal noise counts. The end-on tubes with 2 inch diameter photocathodes were covered with only a central 1/4 inch opening allowing light to pass. Ideally one would like to use identical phototubes to perform this experiment, but in our case, Hamamatsu R1333 and R943 tubes were used. Both tubes could be used in a single photon counting mode and had enhanced red response, although the R943 was more sensitive. The high voltage bias to each tube was adjusted for optimal pulse height distribution.

To properly perform this experiment, both the optical and electrical path after the 50/50 beamsplitter should be exactly equal for the two branches. So far we have discussed the path to the two detectors. The output signal of each detector passed through two stages of amplification providing 25X gain before

being fed to discriminators. Amplifiers were checked to provide equal gain in the two paths by using one EG&G Ortec 574 and one SRS 440 stage in each path. An EG&G Ortec 583 constant fraction differential discriminator was used in each path to remove thermal noise from signal and provide proper pulse shaping for subsequent electronics. As the two PMT's had different photocathode sensitivity, the discriminator levels were adjusted to equalize single channel count rates. All electrical cable lengths were precisely measured and fabricated in duplicate for connecting the above electronics to allow accurate timing. Each discriminator had two identical output channels which were used as follows. One output from each discriminator was connected via 3 dB attenuators to the two input ports of coincidence counter #1 (EG&G C102B/N), with variable time delay inserted into one of the paths. The second output from one discriminator was connected to coincidence counter #2 via a 150 ns delay (provided by an extended length of cable). The second output from the other discriminator was connected via a short cable and a 3 dB attenuator to coincidence counter #2. The 3 dB attenuators in the short cable paths were used to match the attenuation experienced by signals which took the long and winding road (150 ns delay) to coincidence counter #2. Therefore we used coincidence counter #2 to count random coincidences (long time delay path), and coincidence counter #1 to count excess coincidences (variable time delay path). Using ~100 psec mode-locked laser pulses as the light source (i.e. impulse response of system), the time response of the system up to this point was measured on a fast oscilloscope to be approximately 3.5 nsec. Finally the output of each coincidence counter was fed (with 3 dB attenuation) to the dual inputs of a Stanford Research Systems SR400 photon counter unit. The photon counter in this case was used merely as an electronic counter.

With the experimental setup now described, we explain the data acquisition method. First to test the setup we set out to measure the ordinary second order correlation function $(g^{(2)}(\tau)-1)$ for the VCSEL at a fixed pump power below threshold. Thus we expected to see the standard bell shaped curve indicative of bunched light and would allow us to identify the zero time delay point between the two branches of the interferometer. To do this we needed to vary the electronic delay (in approximately nanosecond steps) between the two channels connected to coincidence counter #1. Several methods were tried to provide this variable delay including using a SRS Digital Delay Generator, a Hamamatsu variable delay line box and a homemade delay line box. As it turned out each method had its own problems (discovered after many hours of trial), which resulted in finally implementing the simplest delay line method, i.e. pieces of 50Ω cable cut to exact lengths. We were thus able to obtain a bell shaped curve, albeit somewhat noisy, and able to identify the zero delay point. The extremely high sensitivity of the PMT's to any light required meticulous care be taken to reduce all stray light in the laboratory (even instrumentation indicator lights needed to be covered). It was also necessary that all equipment be turned on and allowed to stabilize for several hours (~5 hours) prior to data taking.

The intent of the experiment was to measure the noise properties of VCSEL light emission during the threshold transition. The procedure for this was slightly different from the test procedure described in the previous paragraph. The pump power was varied by the precision current controlled AOM such that the VCSEL passed from below to above threshold. As shit happens during a momentary lapse of reason, one must be careful not to saturate

the PMT. Thus at each pump power level, the variable neutral density filter was adjusted to keep the single channel count rate at $\sim 10^6$ counts per second. Both random and correlated coincidence count data were recorded at each pump power level for 5 minutes with the entire run taking slightly more than one hour. In order to minimize the need for light while operating the experimental apparatus and to speed the change time between data points, all data and pertinent information were spoken and recorded on an audio microcassette recorder.

Results and Discussion

The measured photon number correlation function is shown by circles in Fig. 3.3 along with the experimental output power versus pump power curve (triangles). To compute the photon statistics, we use the effective experimental values appropriate for the GaAs microcavity laser used in our experiment: they are $N'=2.5 \times 10^7$, $T_2=10^{-13}$ sec, and $g=3.7 \times 10^9$ sec $^{-1}$ ($\rho=4.8 \times 10^{-29}$ mC, $V=25$ μm^3). Furthermore, we express the cavity damping rate κ in terms of its quality factor Q via $\kappa=\omega/Q$, where ω is the angular frequency of the laser transition. From the measured Fabry-Perot width (FWHM) of 1.7\AA , we deduce an effective mirror reflectivity of $R_{\text{eff}}=0.993$. Since the optical field extends well into the Bragg reflectors, the effective cavity length is estimated from multilayer calculations of our microlaser structure to be about 2.2 μm . Thus we obtain $Q \sim 2000$ for the lasing mode given by $Q=\omega L/\text{c} \ln(1/R_{\text{eff}})$. The solid lines in the Fig. 3.3 show the computed K function and output power versus pump power curve (the theory curves are scaled in arbitrary units). The agreement between theory of equation (3.13) and experiment is quite good by using $\beta=6.5 \times 10^{-3}$ ($\gamma=0.8$ GHz) in the calculations, which is more than an order of magnitude larger β than for

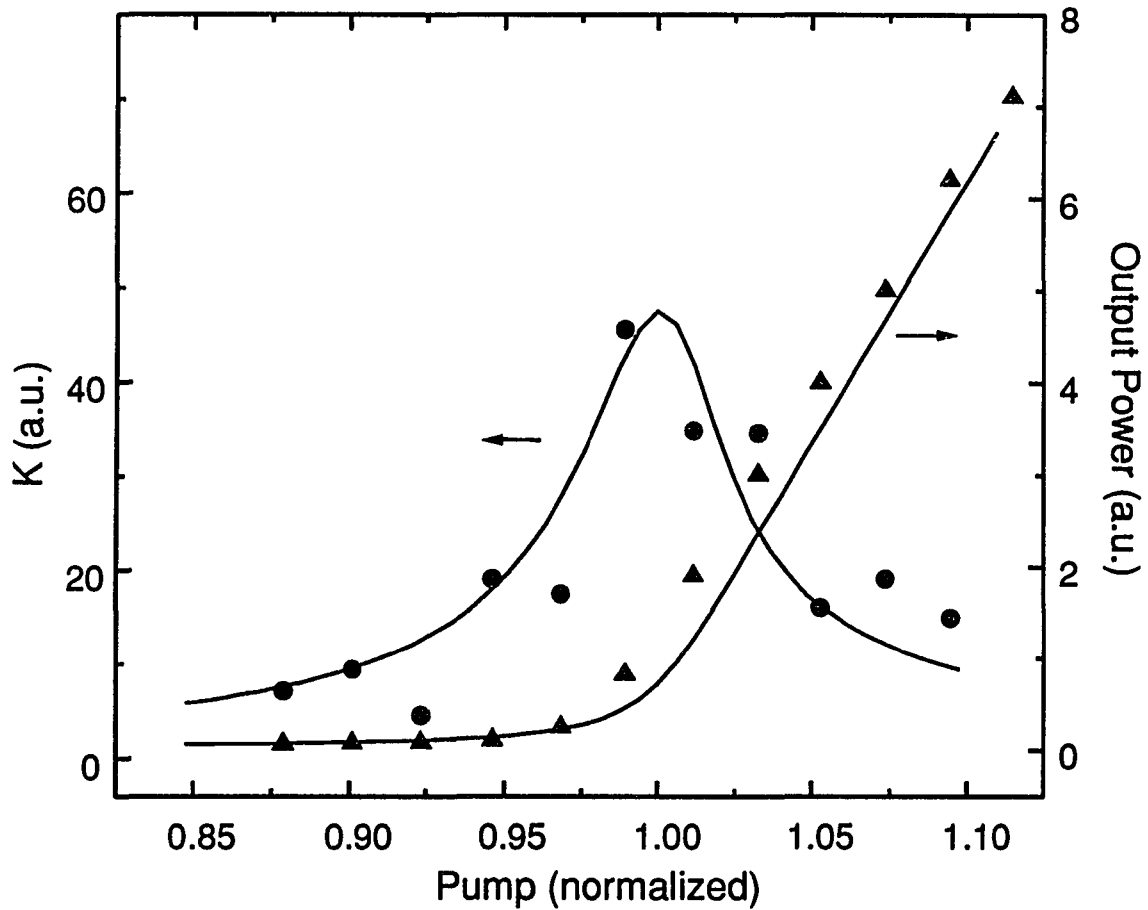


Fig. 3.3 Measured output power (triangles) and photon number fluctuations (circles) of a GaAs microcavity laser. The pump power is normalized such that $\Lambda=1$ corresponds to the peak in the K curve, which is used to define Λ_{th} (Λ_{th} in the experimental curve is ~ 6.8 mW). The solid lines are theoretical plots with parameters $Q=2000$ and $\gamma=0.8$ GHz (corresponding to experimental conditions).

conventional lasers (Whispering gallery mode microdisk lasers are estimated to have $\beta \sim 0.1$, the largest value reported to date [McCall et al. (1992)]).

The theory and experiment of Fig. 3.3 show very similar features although the theory is developed for a simple two-level laser model. The question arises why agreement is observed even though the complex nature of the semiconductor band structure is ignored. This is due to the fact that effective semiconductor medium parameters are used and because the two-level model does describe the tuning-independent features of bulk semiconductor lasers corresponding to those given by the widely used linear density gain model [Yariv (1989)].

The theoretical curves of Fig. 3.4 enable us to compare the derivative-of-intensity threshold with the peak-of-K threshold for very large β . The main result is that the former disappears whereas the Fano-Mandel parameter still clearly exhibits a peak indicative of enhanced intensity fluctuations near threshold. For instance, while the growth in intensity as a function of pump parameter almost follows a straight line in Fig. 3.4c and f , $K(\lambda)$ still exhibits a well-defined peak. We argue that this peak should be used as a proper definition of the threshold of a weak-coupling microlaser. Based on this definition, a microlaser never becomes strictly threshold-less; the quality of the emitted light below the peak-K threshold does not possess the degree of coherence usually associated with laser emission even though the derivative of intensity would make it appear threshold-less.

It is apparent from Fig. 3.4 that threshold defined by peak-K does indeed decrease (but remains finite) as β is increased (γ decreased). This can be explained in terms of a simple physical picture. In the model, the effect of

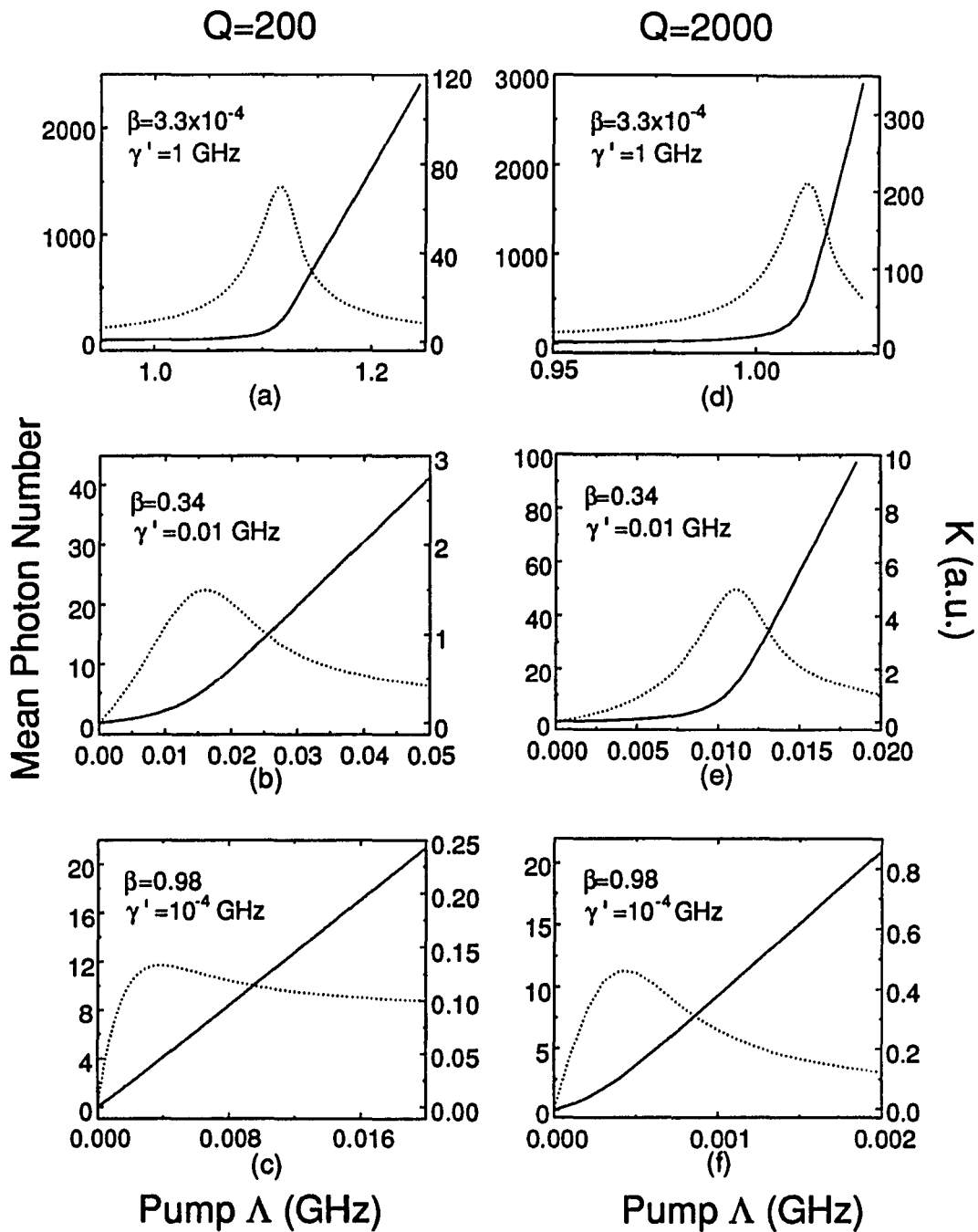


Fig. 3.4 Theoretical average photon number (solid lines) and correlation function K (dotted lines) for various β and Q . Different horizontal and vertical scales are used for clarity. (a)-(c) are for $Q=200$, and (d)-(f) are for $Q=2000$.

suppressed spontaneous emission in a microlaser is a reduction of the "pumping" $N\gamma$ of the lower state population, which in turn, reduces the absorption term B_n . Hence the emission term A_n does not have to compensate for as much absorption, resulting in a reduction of laser threshold. Note also that a population inversion is always necessary to reach threshold (large β does not result in lasing without inversion).

Another interesting outcome of our study is summarized in Fig. 3.5, which shows the normalized second order correlation function $g^{(2)}(0)$ of a microlaser as a function of the β -factor. These results show that as β is increased, $g^{(2)}(0)$ at very low pumping is already less than the thermal source value of 2 and closer to 1 characteristic of Poissonian photon statistics of a coherent state. This is mainly due to the reduction of the number of nonlasing modes which are largely responsible for the intensity noise. Hence, microlasers operating in the weak-coupling regime have reduced (although still classical) intensity fluctuations compared to a standard laser operating at the same pump power. On the other hand it has recently been shown that they also exhibit a larger linewidth [Koch (1993)]. We are, then, led to the conclusion that although microlasers are difficult to distinguish from light emitting diodes (LED) from their spectral characteristics, their higher-order correlation functions, which demonstrate a high degree of second-order coherence, are fundamentally different. It should be noted that the reduced value of $g^{(2)}(0)$ below threshold, however, is still much larger than that of a highly coherent light source, such as in the case of a conventional laser above threshold. Thus the determination of the threshold of microcavity lasers by the peak of the Fano-Mandel parameter is of

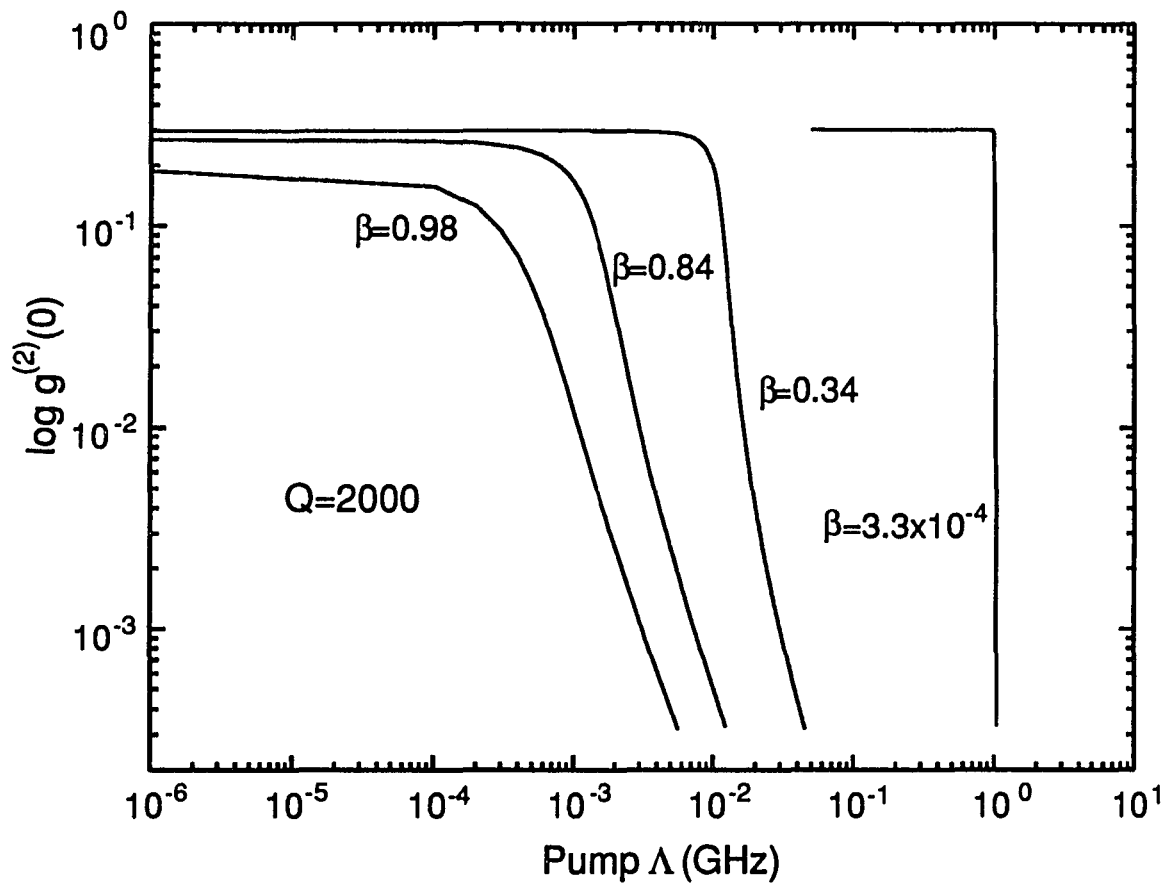


Fig. 3.5 Calculated second order coherence function $g^{(2)}(0)$ as a function of pump power for various β .

great importance in practical situations that require a high degree of second-order coherence.

Summary

We have outlined the quantum theory of a weak-coupling microlaser and compared it with experiments. We found good agreement between the predicted and measured values of the second-order correlation of the field for low β . The theoretical results for high β values stress the importance of using the peak in the Fano-Mandel parameter of the field as a definition of microlaser threshold. The threshold-less laser is a fiction if second order coherence (intensity noise) is the criterion. We have also shown that while the spectral properties of these lasers, which resemble those of LEDs, make them of questionable use in interferometric-type applications, they exhibit a strong degree of second-order coherence as a function of pump rate, and might be of considerable interest in amplitude-modulation type applications.

CONCLUSION

Innovations in semiconductor growth and fabrication technology have led to the birth and development of the microcavity laser. In the hands of an engineer, a plethora of applications of this new laser structure may come to fruition. In the hands of a physicist, a microcavity laser becomes a tool to further understanding of basic science. Thus, the microcavity laser is a unique example of technology fostering scientific progress. We have expressly studied the microcavity laser from the physics viewpoint (this evidenced by a simple calculation: typical microcavity laser volume $\equiv 1 \text{ gnome} \sim 10^{-10} \text{ cm}^3$; estimated volume of experimental apparatus only $> 50 \text{ ft}^3 \sim 10^{16} \text{ gnomes}$; Sixteen orders of magnitude larger!).

By injecting an external laser signal into a free-running VCSEL we have observed the low injection regime of frequency locking and the high injection regime of asymmetric local gain modification. The low injection nonlinear dynamical behavior is well modeled by standard coupled rate equations. The high injection asymmetric gain modification is explained by coherent energy transfer through injection induced population pulsations (cavity enhanced optical fields increase stimulated processes allowing the large observed frequencies).

From an above threshold measurement of linewidth and injection locking range we have determined the linewidth enhancement factor, in good agreement with theory. From simple below threshold measurements we are able to get some idea of carrier density and carrier lifetime. These measurements allow us

to give values for operating parameters of microcavity lasers not previously known.

Measurement of the field second order correlation function exhibits a peak at threshold. Calculations based on a quantum two-level laser theory agree with experiment and further show that this peak persists even as the spontaneous emission rate into nonlasing modes approaches zero. Thus, the correlation function peak provides a universal definition of laser threshold.

We take this final opportunity to offer a few observations on the current status of the field. With solid state physicists talking about quantum dot "artificial atoms" and atomic physicists discussing lattices and band structure, a cursory glance might lead an observer to proclaim "Meshugeneh velt!" (Crazy world!). However, more careful thought reveals a beautiful symbiosis rarely seen in an era of sub-...-sub-specialization in physics. Localization in solid state physics (i.e. Anderson localization) spawned the idea of localization of light and the idea of the photonic bandgap. Asymmetric gain modification in semiconductors, presented here, was motivated in part by previous work on driven atomic systems. Laser cooling of atoms has led to optical molasses and the realization of an atomic lattice held together by light forces. Electrons are beginning to be treated as waves in semiconductor heterostructures, and atom optics has led to demonstration of interference of the atomic wavepacket. The solid state quantum dot may one day yield discrete atomic-like spectra. Ideas of cavity QED and modified spontaneous emission rates first studied in atomic systems (for example the micromaser) have now begun to make an impact in the semiconductor microcavity community. Our study of laser threshold was

motivated by the desire to understand the threshold-less laser concept, which itself was inspired by the concept of inhibited spontaneous emission.

Pages too many have turned already (beginning with BS, we added more and more of it, progressively piling it higher and deeper until impenetrable), thus we stop here.

REFERENCES

- Adachi, S., *J. Appl. Phys.* **58**, R1 (1985).
- Agrawal, G. P., Dutta, N. K., *Long-Wavelength Semiconductor Lasers* (Van Nostrand, 1986).
- Agrawal, G. P., Roy, R., *Phys. Rev. A* **37**, 2495, (1988a).
- Agrawal, G. P., *J. Opt. Soc. Am. B* **5**, 147 (1988b).
- Armstrong, J. A., Smith, A. W., *Phys. Rev. Lett.* **14**, 68 (1965a).
- Armstrong, J. A., Smith, A. W., *Phys. Rev.* **140**, 155 (1965b).
- Baba, T., Hamano, T., Koyama, F., Iga, K., *IEEE J. Quant. Electron.* **27**, 1347 (1991).
- Baba, T., Hamano, T., Koyama, F., Iga, K., *IEEE J. Quant. Electron.* **28**, 1310 (1992).
- Banyai, L., Koch, S. W., *Z. Physik B* **63**, 283 (1986).
- Binder, R., Scott, D., Paul, A. E., Lindberg, M., Hennenberger, K., Koch, S. W., *Phys. Rev. B* **45**, 1107 (1992).
- Bjork, G., Yamamoto, Y., *IEEE J. Quant. Electron.* **27**, 2386 (1991).
- Bogatov, A. P., Eliseev, P. G., Sverdlov, B. N., *IEEE J. Quant. Electron.* **QE-11**, 510, (1975).
- Boggavarapu, D., Jin, R., Grantham, J., Hu, Y. Z., Brown de Colstoun, F., Lowry, C. W., Khitrova, G., Koch, S. W., Sargent III, M., Gibbs, H. M., accepted for publication *Opt. Lett.* (1993).
- Born, M., Wolf, E., *Principles of Optics*, 6th. ed. (Pergamon Press, 1986).
- Carmichael, H. J., Brecha, R. J., Raizen, M. G., Xiao, M., Kimble, H. J., *J. Opt. Soc. Am. B* **3**, 238 (1986).

REFERENCES - *Continued*

- Chavez-Pirson, A., Ph.D. dissertation, University of Arizona, (1989).
- Chinn, S. R., *Appl. Phys. Lett.* **59**, 1673 (1991).
- Chuang, C. L., Ph.D. dissertation, University of Arizona, (1991).
- Cohen-Tannoudji, C., Dupont-Roc, J., Grynberg, G., *Photons and Atoms* (John Wiley, 1989).
- de Giorgio, V., Scully, M. O., *Phys Rev. A* **2**, 1170 (1970).
- De Martini, F., Jacobovitz, G. R., *Phys. Rev. Lett.* **60**, 1711 (1988).
- De Martini, F., Marrocco, M., Mataloni, P., Crescenti, L., Loudon, R., *Phys. Rev. A* **43**, 2480 (1991).
- Gabrielse, G., Dehmelt, H., *Phys. Rev. Lett.* **55**, 67 (1985).
- Gibbs, H. M., *Optical Bistability: Controlling Light with Light* (Academic Press, 1985).
- Glauber, R. J., in *Quantum Optics and Electronics*, C. DeWitt, A. Blandin, C. Cohen-Tannoudji, eds., (Gordon and Breach, 1965).
- Graham, R., Haken, H., *Z. Physik* **237**, 31 (1970).
- Grantham, J. W., Ph.D. dissertation, University of Arizona, (1991).
- Haken, H., *Light* (North Holland, 1985).
- Hanbury-Brown, R., Twiss, R. Q., *Proc. Roy. Soc. A* **243**, 291 (1958).
- Hanbury-Brown, R., *The Intensity Interferometer* (Taylor and Francis, 1974).
- Haroche, S., Hartman, F., *Phys. Rev. A* **6**, 1280 (1972).
- Haroche, S., in *Fundamental Systems in Quantum Optics*, J. Dalibard, J. M. Raimond, J. Zinn-Justin, eds., (North-Holland, 1992).

REFERENCES - *Continued*

- Haug, H., Haken, H., *Z. Physik* **204**, 262 (1967).
- Haug, H., Koch, S. W., *Quantum Theory of the Optical and Electronic Properties of Semiconductors* (World Scientific, 1990).
- Heinzen, D. J., Childs, J. J., Thomas, J. E., Feld, M. S., *Phys. Rev. Lett.* **58**, 1320 (1987a).
- Heinzen, D. J., Feld, M. S., *Phys. Rev. Lett.* **59**, 2623 (1987b).
- Henry, C. H., Logan, R. A., Merrit, F. R., *J. Appl. Phys.* **51**, 3042 (1980).
- Henry, C. H., *IEEE J. Quant. Electr.* **QE-18**, 259 (1982).
- Hui, R., D'Ottavi, A., Mecozzi, A., Spano, P., *IEEE J. Quant. Electron.* **27**, 1688 (1991).
- Hulet, R. G., Hilfer, E. S., Kleppner, D., *Phys. Rev. Lett.* **55**, 2137 (1985).
- Jewell, J. L., Harbison, J. P., Scherer, A., Lee, Y. H., Florez, L. T., *IEEE J. Quant. Electron.* **27**, 1332, (1991).
- Jin, R., unpublished (1991).
- Jin, R., Boggavarapu, D., Khitrova, G., Gibbs, H. M., Hu, Y. Z., Koch, S. W., Peyghambarian, N., *Appl. Phys. Lett.* **61**, 1883 (1992).
- Jin, R., Boggavarapu, D., Sargent III, M., Meystre, P., Gibbs, H. M., Khitrova, G., submitted to *Phys. Rev. Lett.* (1993).
- Khitrova, G., Berman, P., Sargent III, M., *J. Opt. Soc. Am. B* **5**, 160 (1988a).
- Khitrova, G., Valley, J. F., Gibbs, H. M., *Phys. Rev. Lett.* **60**, 1126 (1988b).
- Kikuchi, K., Kakui, M., Zah, C., Lee, T., *IEEE J. Quant. Electron.* **28**, 151 (1992).
- Kleppner, D., *Phys. Rev. Lett.* **47**, 233 (1981).

REFERENCES - *Continued*

- Kobayashi, S., in *Coherence, Amplification, and Quantum Effects in Semiconductor Lasers*, Y. Yamamoto, ed., (John Wiley, 1991), pp. 367-410.
- Koch, S. W., *Bull. Am. Phys. Soc.* **38**, 98 (1993).
- Lang, R., *IEEE J. Quant. Electron.* **QE-18**, 976 (1982).
- Lax, M., *Phys. Rev.* **157**, 213 (1967).
- Lee, Y. H., Chavez-Pirson, A., Koch, S. W., Gibbs, H. M., Park, S. H., Morhange, J., Peyghambarian, N., Banyai, L., Gossard, A. C., Weigmann, W., *Phys. Rev. Lett.* **57**, 2446 (1986a).
- Lee, Y. H., Chavez-Pirson, A., Rhee, B. K., Gibbs, H. M., Gossard, A. C., Wiegmann, W., *Appl. Phys. Lett.* **49**, 1505 (1986b).
- Lin, J., Gamelin, J. K., Lau, K., Y., Wang, S., Hong, M., Mannaerts, J. P., *Appl. Phys. Lett.* **60**, 15 (1992).
- Lindberg, M., An, S., Koch, S. W., Sargent III, M., *Phys. Rev. A* **40**, 4415 (1989).
- Loudon, R., *The Quantum Theory of Light*, 2nd ed. (Clarendon Press, 1983).
- Lowry, C. W., Brown de Colstoun, F., Paul, A. E., Khitrova, G., Gibbs, H. M., Grantham, J. W., Jin, R., Boggavarapu, D., Koch, S. W., Sargent III, M., Brennan, T. M., Hammons, B. E., submitted to *Phys. Rev. Lett.* (1993).
- Maiman, T. H., *Nature* **187**, 493 (1960).
- Mandel, L., *Opt. Commun.* **42**, 356 (1982).
- McCall, S. L., Levi, A. F. J., Slusher, R. E., Pearton, S. J., Logan, R. A., *Appl. Phys. Lett.* **60**, 289 (1992).
- Meschede, D., Walther, H., Muller, G., *Phys. Rev. Lett.* **54**, 551 (1985).
- Meystre, P., Sargent III, M., *Elements of Quantum Optics*, 2nd ed. (Springer-Verlag, 1991).

REFERENCES - *Continued*

- Meystre, P., in *Progress in Optics* Vol. XXX, E. Wolf, ed. (Elsevier, 1992).
- Mogensen, F., Olesen, H., Jacobsen, G., IEEE J. Quant. Electron. **QE-21**, 784 (1985).
- Mollow, B. R., Phys. Rev. **188**, 1969 (1969).
- Nietze, R., Elsasser, W., Baranov, A. N., Wunstel, K., Appl. Phys. Lett. **58**, 554, (1991).
- Olshansky, R., Su, C. B., Manning, J., Powazinik, W., IEEE J. Quant. Electron. **QE-20**, 838 (1984).
- Osinski, M., Buus, J., IEEE J. Quant. Electr. **QE-23**, 9 (1987).
- Oudar, J. L., Kuszelewicz, R., Sfez, B., Michel, J. C., Planel, R., Opt. Quant. Electron. **24**, S193-S207, (1992).
- Paul, A. E., Lindberg, M., An, S., Sargent III, M., Koch, S. W., Phys. Rev. A **42**, (1990).
- Petitbon, I., Gallion, P., DeBarge, G., Chabran, C., IEEE J. Quant. Electron. **24**, 148 (1988).
- Pon, R. M., Ph.D. dissertation, University of Arizona, (1991).
- Provost, J. G., Frey, R., Appl. Phys. Lett. **55**, 519 (1989).
- Purcell, E. M., Phys. Rev. **69**, 681 (1946).
- Raizen, M. G., Brecha, R. J., Kimble, H. J., Carmichael, H. J., Phys. Rev. Lett. **63**, 240 (1989).
- Saitoh, T., Mukai, T., in *Coherence, Amplification, and Quantum Effects in Semiconductor Lasers*, Y. Yamamoto, ed., (John Wiley, 1991), pp. 257-322.
- Sargent III, M., Scully, M. O., Lamb Jr., W. E., *Laser Physics* (Addison-Wesley, 1974).

REFERENCES - *Continued*

- Sargent III, M., Zhou, F., Koch, S. W., Phys. Rev. A **38**, 4673, (1988).
- Sargent III, M., Paul, A. E., Koch, S. W., submitted to Opt. Commun. (1993).
- Schawlow, A. L., Townes, C. H., Phys. Rev. **112**, 1940 (1958).
- Scully, M. O., Lamb Jr., W. E., Phys. Rev. **159**, 208 (1967).
- Siegman, A. E., *Lasers*, (University Science Books, 1986), Chap. 29.
- Spencer, M. B., Lamb Jr., W. E., Phys. Rev. **A5**, 884 (1972).
- Suematsu, Y., Furuya, K., Trans. IECE Japan **E 60**, 467 (1977).
- Tiemeijer, L. F., Appl. Phys. Lett. **59**, 499 (1991).
- Weisbuch, C., Niskioka, M., Ishikawa, A., Arakawa, Y., Phys. Rev. Lett. **69**, 3314 (1992).
- Wu, F. Y., Ezekiel, S., Ducloy, M., Mollow., Phys. Rev. Lett. **38**, 1077 (1977).
- Yablonovitch, E., Phys. Rev. Lett. **58**, 2059 (1987).
- Yablonovitch, E., Gmitter, T. J., Bhat, R., Phys. Rev. Lett. **61**, 2546 (1988).
- Yablonovitch, E., Gmitter, T. J., Phys. Rev. Lett. **63**, 1950 (1989).
- Yamamoto, Y., Machida, S., Bjork, G., Opt. Quant. Electron. **24**, S215-S243 (1992).
- Yariv, A., Yeh, P., *Optical Waves in Crystals* (John Wiley, 1984).
- Yariv, A., *Quantum Electronics*, 3rd ed. (John Wiley, 1989).
- Yokoyama, H., Brorson, S. D., J. Appl. Phys. **66**, 4801 (1989).
- Zhou, F. L., Sargent III, M., Koch, S. W., Chow, W. W., Phys. Rev. A **41**, 463 (1990).